

**Measurement of differential cross sections of the Σ^+p
elastic scattering in momentum range of
0.44 – 0.80 GeV/c**

T. Nanamura^{1,2}, K. Miwa³, J. K. Ahn⁴, Y. Akazawa⁵, T. Aramaki³,
S. Ashikaga¹, S. Callier⁶, N. Chiga³, S. W. Choi⁴, H. Ekawa⁷,
P. Evtoukhovitch⁸, N. Fujioka³, M. Fujita², T. Gogami¹, T. K. Harada^{1,2},
S. Hasegawa², S. H. Hayakawa³, R. Honda⁵, S. Hoshino⁹, K. Hosomi²,
M. Ichikawa^{1,2}, Y. Ichikawa², M. Ieiri⁵, M. Ikeda³, K. Imai², Y. Ishikawa³,
S. Ishimoto⁵, W. S. Jung⁴, S. Kajikawa³, H. Kanauchi³, H. Kanda¹⁰,
T. Kitaoka³, B. M. Kang⁴, H. Kawai¹¹, S. H. Kim⁴, K. Kobayashi⁹,
T. Koike³, K. Matsuda³, Y. Matsumoto³, S. Nagao³, R. Nagatomi⁹,
Y. Nakada⁹, M. Nakagawa⁷, I. Nakamura⁵, M. Naruki^{1,2}, S. Ozawa³,
L. Raux⁶, T. G. Rogers³, A. Sakaguchi⁹, T. Sakao³, H. Sako², S. Sato²,
T. Shiozaki³, K. Shiotori¹⁰, K. N. Suzuki¹, S. Suzuki⁵, M. Tabata¹¹,
C. d. L. Taille⁶, H. Takahashi⁵, T. Takahashi⁵, T. N. Takahashi¹²,
H. Tamura^{2,3}, M. Tanaka⁵, K. Tanida², Z. Tsamalaidze^{8,13}, M. Ukai^{3,5},
H. Umetsu³, S. Wada³, T. O. Yamamoto², J. Yoshida³, and K. Yoshimura¹⁴

¹*Department of Physics, Kyoto University, Kyoto 606-8502, Japan*

²*Advanced Science Research Center (ASRC), Japan Atomic Energy Agency
(JAEA), Tokai, Ibaraki 319-1195, Japan*

³*Department of Physics, Tohoku University, Sendai 980-8578, Japan*

⁴*Department of Physics, Korea University, Seoul 02841, Korea*

⁵*Institute of Particle and Nuclear Studies (IPNS), High Energy Accelerator
Research Organization (KEK), Tsukuba 305-0801, Japan*

⁶*OMEGA Ecole Polytechnique-CNRS/IN2P3, 3 rue Michel-Ange, 75794
Paris 16, France*

⁷*High Energy Nuclear Physics Laboratory, RIKEN, Wako, 351-0198, Japan*

⁸*Joint Institute for Nuclear Research (JINR), Dubna, Moscow Region
141980, Russia*

⁹*Department of Physics, Osaka University, Toyonaka 560-0043, Japan*

¹⁰*Research Center for Nuclear Physics (RCNP), Osaka University, Ibaraki
567-0047, Japan*

¹¹*Department of Physics, Chiba University, Chiba 263-8522, Japan*

¹²*Nishina Center for Accelerator-based Science, RIKEN, Wako, 351-0198,
Japan*

¹³*Georgian Technical University (GTU), Tbilisi, Georgia*

¹⁴*Department of Physics, Okayama University, Okayama 700-8530, Japan*

**E-mail: nanamura@scphys.kyoto-u.ac.jp*

.....
We performed a novel Σp scattering experiment at the J-PARC hadron experimental facility. Approximately 2400 $\Sigma^+ p$ elastic scattering events were identified by requesting the kinematical consistency of the elastic scattering from 4.9×10^7 tagged Σ^+ beam particles in the Σ^+ momentum range of 0.44 – 0.80 GeV/c. The differential cross sections of the $\Sigma^+ p$ elastic scattering were derived with much better precision compared to past experiments. The obtained values of differential cross sections are around 2 mb/sr, which are not so large as most theoretical predictions. Moreover, the phase shifts of 3S_1 and 1P_1 channels were experimentally derived for the first time. The phase shift of the 3S_1 channel wherein a large repulsive core was predicted owing to the Pauli effect in the quark level was evaluated to be $20^\circ < |\delta_{^3S_1}| < 35^\circ$. If the sign is assumed to be negative, the strength of the interaction in this channel was found to be moderately repulsive.
.....

Subject Index xxx, xxx

1 Introduction

The understanding of the origin of short-range repulsion in nuclear force is an important challenge in nuclear physics. In pioneering researches on the nuclear force, the short-range repulsion was phenomenologically treated [1] or was attributed to the ω exchange in boson-exchange picture [2]. The effect of antisymmetrization among quarks at the short-range interaction was first considered using the quark cluster model (QCM) by Oka and Yazaki [3, 4]. They reported that the short-range repulsion could be explained by the Pauli principle between quarks, called quark Pauli effect, and color-magnetic interaction.

By extending the nuclear force (NN interaction) to the baryon-baryon (BB) interaction between octet baryons comprising $u, d,$ and s quarks ($n, p, \Lambda, \Sigma^\pm, \Sigma^0, \Xi^-, \Xi^0$), the contributions of the quark Pauli effect and color-magnetic interaction to the BB interaction can be multidirectionally examined [5]. The BB interactions between octet baryons are labeled by irreducible flavor multiplets as

$$\mathbf{8} \otimes \mathbf{8} = \mathbf{27} \oplus \mathbf{8}_s \oplus \mathbf{1} \oplus \mathbf{10}^* \oplus \mathbf{10} \oplus \mathbf{8}_a. \quad (1)$$

The relationship between isospin and flavor SU(3) bases for the two-baryon system with strangeness 0 and -1 are summarized in Table 1. Although the 27-plet and 10*-plet can be examined from the NN interactions, the other four multiplets can be studied only from hyperon-nucleon (YN) and hyperon-hyperon (YY) interactions. They are expected to have different features from the NN interaction at a short-range region. For example, the 8_s -plet and 10-plet are predicted to have a quite large repulsive force due to the quark Pauli effect. In contrast to them, the 8_a -plet and 1-plet are expected to have an extremely weak core and attractive pocket, respectively, because of the color-magnetic interaction. Therefore, revealing the natures of the flavor SU(3) multiplets is important for the systematic understanding of the BB interactions. In the ΣN channels, five flavor SU(3) multiplets except for the 1-plet are included. Especially, the $\Sigma^+ p$ and $\Sigma^- n$ channels are the pure isospin $I = 3/2$ states, and their 3 even and 1 odd states¹ are suitable to investigate the 10-plet. The contributions of these states can be extracted from spin-averaged interaction because their 1 even and 3 odd states are estimated from the NN ($I = 1$) interaction based on the flavor SU(3) symmetry.

The theoretical treatment of the short-range interaction in the BB interactions had led to considerably different results on the ΣN ($I = 3/2, ^3S_1$) interaction. The fss2, which includes QCM in the short-range region and the empirical meson-exchange potential in the middle- and long-range regions, naturally predicts a considerably repulsive interaction in the ΣN

¹ In this study, the spin state (singlet or triplet) and parity of orbital angular momentum are represented using this notation

Table 1: Relationship between the isospin and flavor SU(3) bases for the BB interaction channels.

strangeness	BB channel (I)	1 even or 3 odd	3 even or 1 odd
0	$NN(I = 0)$	–	(10*)
	$NN(I = 1)$	(27)	–
–1	$\Lambda N(I = \frac{1}{2})$	$\frac{1}{\sqrt{10}}[(\mathbf{8}_s) + 3(\mathbf{27})]$	$\frac{1}{\sqrt{2}}[-(\mathbf{8}_a) + (\mathbf{10}^*)]$
	$\Sigma N(I = \frac{1}{2})$	$\frac{1}{\sqrt{10}}[3(\mathbf{8}_s) - (\mathbf{27})]$	$\frac{1}{\sqrt{2}}[(\mathbf{8}_a) + (\mathbf{10}^*)]$
	$\Sigma N(I = \frac{3}{2})$	(27)	(10)

($I = 3/2, ^3S_1$) channel [6]. However, the meson-exchange models, such as Nijmegen Soft Core (NSC) model [7, 8] and Jülich YN model A [9], which represent the short-range interaction from a heavy vector-meson exchange, cannot predict such a large repulsive force. The Nijmegen NSC97 model, whose ΛN interaction is extensively used for Λ hypernuclear studies, predicts an attractive interaction for the ΣN ($I = 3/2, ^3S_1$) channel [8]. Experimental information about the ΣN interaction in the nuclear core region was quite limited because of the no observation of Σ hypernuclei except for $^4_{\Sigma}\text{He}$ [10]. However, the quasifree Σ^- production spectra in medium nuclei obtained at KEK-PS demonstrated that the spin-isospin averaged Σ potential has a strong repulsion in the real part with a sizable absorption in the imaginary part [11, 12], and this nature was confirmed for even the $\Sigma^- + ^5\text{He}$ system [13, 14]. From these experimental results, the ΣN ($I = 3/2, ^3S_1$) channel is believed to be repulsive. In the Nijmegen Extended Soft Core (ESC) model, an additional short-range interaction owing to Pomeron exchange is included to explain the repulsive nature of the ΣN ($I = 3/2, ^3S_1$) channel [15, 16]. The potentials of the BB S -wave interaction in the flavor-irreducible representation were calculated from a lattice QCD simulation in the flavor SU(3) limit, and the potential shapes agree with the QCM prediction [17]. Further, the ΣN ($I = 3/2, ^3S_1$) potential derived by the lattice QCD simulation in the almost physical quark masses demonstrated a repulsive core in the short-range region without any attractive pocket in the middle-range region [18]. Recent calculations by chiral effective field theory (χ EFT), extended to the YN sectors, predict repulsive interaction for this channel [19, 20]. In a χ EFT calculation, the short-range interaction is treated as contact interaction represented by low energy constants (LECs).

Currently, all theoretical calculations predict repulsive interactions in the ΣN ($I = 3/2, ^3S_1$) channel. However, the strength of the repulsive interaction, i.e., the phase shift value

of the 3S_1 channel, is quite different from each other; this strength should be experimentally determined. The theoretical predictions of the differential cross section in the intermediate momentum region above 0.4 GeV/ c differ among themselves depending on the size of the repulsion of the 3S_1 channel [6, 15, 16, 19, 20]. Therefore, the accurate determination of the differential cross sections of the Σ^+p channel plays a crucial role in determining the strength of the repulsive interaction. Moreover, because of the simple representation of the multiplet, one can experimentally derive the phase shift of the 10-plet from a numerical phase shift analysis of the differential cross section with some assumptions as explained in Section 5. To date, no phase shift values of the YN and YY channels have been experimentally determined. This is unlike the NN interaction, of which phase shifts were precisely determined from the scattering observables of pp and np scatterings [21].

The BB interactions are essential information to predict the onset of hyperons in neutron stars [22]. Recently, the particle composition in the high-density region at the inner core of neutron stars has been discussed to consider the mechanism to support massive neutron stars with two-solar mass. Because the onset of the Σ^- permits a proton's appearance owing to the charge neutrality, the Σ^- 's impact on the particle composition is considerably large. Although the Σ potential in the symmetric nuclear matter is estimated from Σ^- quasifree production data in the medium heavy nuclei, the Σ^- potential in the neutron matter is an important information for studies of neutron stars. The Σ^-n interaction, which is equal to the Σ^+p interaction from isospin symmetry, is an important input to obtain the Σ^- potential in the neutron matter using G-matrix calculations [23]. Therefore, the investigation of the Σ^+p interaction is essential to determine the nature of Σ^- in neutron stars.

As for the experimental situation of the YN scatterings, historically, the YN scattering data are considerably scarce because of the experimental difficulties caused by the short lifetime of hyperons [24–32]. In the intermediate energy, two experiments have been performed [32, 33] to measure the differential cross sections of the Σ^+p channel. They could not draw any conclusion on the repulsive nature because of the insufficient accuracy stemming from low statistics. Although there is one spin-observable measurement on the Σ^+p channel [34], the information about the Σ^+p scattering is quite limited. Furthermore, we, J-PARC E40 collaboration, have recently succeeded in the systematic measurements of $\Sigma^\pm p$ scatterings with high statistics at J-PARC. The Σ^-p results can be found in [35, 36]. In this study, we report the results of the differential cross section measurements of the Σ^+p elastic scattering in the Σ^+ momentum range of 0.44 – 0.80 GeV/ c .

2 Experiment

We performed the Σp scattering experiment, J-PARC E40, at the K1.8 beam line [37] in the J-PARC Hadron Experimental Facility, where mass-separated secondary hadron beams produced by exposing a primary Au target to a 30-GeV primary proton beam extracted from the J-PARC main ring are delivered to experimental areas. The spill cycle and beam duration in the accelerator operation were 5.2 and 2 s, respectively. The experimental concept and setup of the Σp scattering experiment are shown in Fig. 1. A high intensity π^+ beam of approximately $2 \times 10^7/\text{spill}$ was used to produce many Σ^+ particles inside a liquid hydrogen (LH_2) target via the $\pi^+ p \rightarrow K^+ \Sigma^+$ reaction. The central momentum of the beam was 1.41 GeV/c. After the production, the Σ^+ particles traveled in the LH_2 target during the lifetime. Such Σ^+ particles were regarded as “ Σ^+ beam.” The $\Sigma^+ p$ scattering could occur during the Σ^+ 's flight in the LH_2 target.

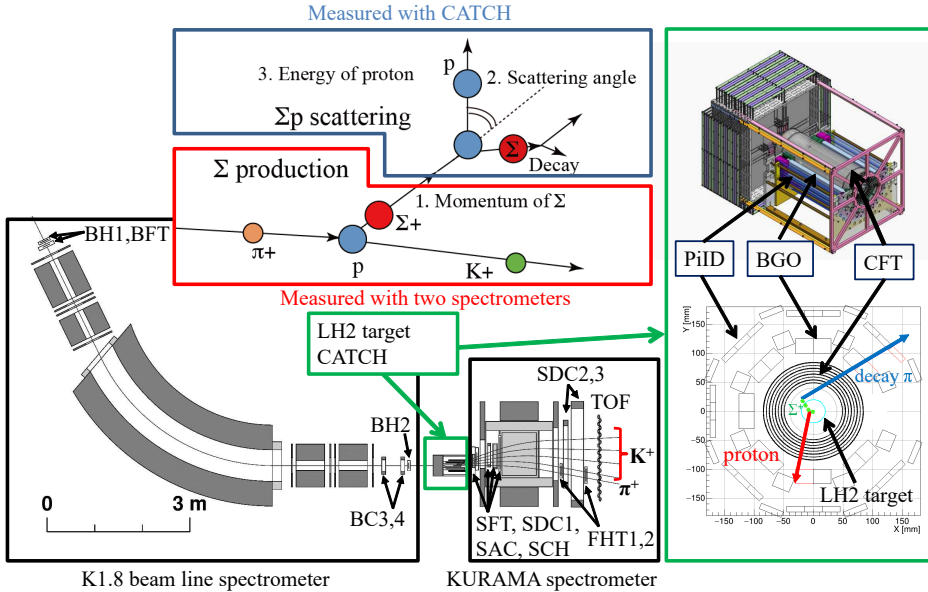


Fig. 1: Experimental concept and setup of the Σp scattering experiment. The K1.8 beam line spectrometer comprises five analyzer magnets in a QDQD configuration, two hodoscopes (BH1 and BH2) and three tracking detectors (BFT, BC3, and BC4). In the KURAMA spectrometer, seven tracking detectors (SFT, SCH, SDC1, SDC2, SDC3, FHT1, and FHT2) and two counters (SAC and TOF) are used. The Σ^+ production reaction, namely the $\pi^+ p \rightarrow K^+ \Sigma^+$ reaction, is analyzed using the two spectrometers. CATCH, which comprises CFT, BGO, and PiID surrounds the LH_2 target and measures charged particles involved in the Σ^+ -induced reactions: Recoil proton of $\Sigma^+ p$ scattering and decay products of Σ^+ , and so on.

The momentum of each Σ^+ can be calculated as the missing momentum of the π^+ beam and scattered K^+ analyzed using the K1.8 beam line spectrometer and forward magnetic spectrometer (KURAMA spectrometer). The LH₂ target was surrounded by Cylindrical Active Tracker and Calorimeter system for Hyperon-proton scattering (CATCH), which comprised a cylindrical fiber tracker (CFT), a BGO calorimeter (BGO), and a plastic scintillator hodoscope (PiID) [38], as shown in the right side of Fig. 1. The momentum vector of the recoil proton is determined using CATCH. Then, the Σ^+p scattering events can be kinematically identified from the momentum vectors of the Σ^+ beam and recoil proton in the Σ^+p scattering. The spectrometers and CATCH are described in detail in the following paragraphs. The effective areas and position resolutions of detectors in the spectrometers are summarized in Table 2.

Table 2: Effective areas and position resolutions of detectors.

Detector	role	effective area H \times V [mm ²]	σ_{pos} [mm]
BH1	(BFT hits selection)	170 \times 90	–
BFT	tracker	160 \times 80	0.19
BC3,4	tracker	200 \times 100	0.20
BH2	trigger	118 \times 60	–
SFT	trigger, tracker	280 \times 160	0.18
SDC1	tracker	380 \times 264	0.30
SAC	trigger	484 \times 402	–
SCH	trigger, tracker	673 \times 450	6.0
FHT1	tracker	196 \times 450	0.58
SDC2	tracker	1185 \times 1185	0.40
SDC3	tracker	1920 \times 1280	0.40
FHT2	tracker	256 \times 450	0.58
TOF	trigger, (tracker)	1800 \times 1800	40(H), 20(V)

The π^+ beam was focused on the LH₂ target via a set of QQDQQ magnets at the most downstream of the K1.8 beam line. These magnets form the K1.8 beam line spectrometer together with detectors that were installed upstream and downstream of the magnets. A hodoscope (BH1) and a fiber tracking detector (BFT [39]) were placed upstream of the magnets. On the other hand, drift chambers (BC3 and BC4) and a hodoscope (BH2) were

placed downstream of these magnets. BH2 determined origin of the timing for all detectors. The typical timing resolution of the beam time-of-flight (ToF) between BH1 and BH2 of 10.4-m apart was 300 ps in σ . Although the beam ToF is usually used for the beam particle identification, the contaminations of other particle species in the beam were negligibly small in this experiment owing to the two electro-static separators equipped along the K1.8 beam line. Thus, BH1, which comprised 11 segments of scintillator, was primarily used for selecting the BFT hits corresponding to the triggered event in multiple-beam events. The π^+ beam momentum was reconstructed event-by-event using the spatial information from BFT, BC3, BC4, and the third-order transfer-matrix calculated by ORBIT [40].

The LH₂ was filled in a target container of a cylinder having a 40-mm diameter and 300-mm length with half-sphere end-caps for both edges. A vacuum window around the target region was made by a CFRP cylinder having an 80-mm diameter and 1-mm thickness.

The outgoing particles produced at the LH₂ target by the π^+p reaction were analyzed using the KURAMA spectrometer at the downstream of the LH₂ target. The KURAMA spectrometer comprised a dipole magnet, a fiber tracker (SFT), fine segmented hodoscopes (SCH, FHT1, and FHT2), three drift chambers (SDC1, SDC2, and SDC3), and two counters (TOF and SAC). The KURAMA magnet was excited to 0.78 T at the central position. SFT, SDC1, SAC, and SCH were placed at the entrance or inside of the KURAMA magnet gap. SDC2, SDC3, FHT1, FHT2, and TOF were installed downstream of the magnet. The trajectories of charged particles in the magnetic field were reconstructed by the Runge-Kutta method [41], and their momenta were obtained as the optimal momenta, with which the measured hit positions at the tracking detectors were reproduced. The ToF of the outgoing particle along the flight path of approximately 3-m distance was measured with the TOF counter. The typical time resolution was 300 ps. The spectrometer acceptance for K^+ in the $\pi^+p \rightarrow K^+\Sigma^+$ reaction was approximately 6.7%, and the survival rate of K^+ was 65%. The large acceptance and short flight length were advantages of the KURAMA spectrometer to accumulate many Σ^+ particles.

The high-rate π^+ beam particles penetrated the KURAMA spectrometer, which covered the forward region. To stably operate the detectors and suppress triggers caused by unexpected beam interaction under such an experimental condition, we implemented countermeasures against this limitation. The KURAMA magnet was placed in a horizontally shifted position from the beam axis to cover only the left-sided scattered particles from 3 to 30 degrees. Tracking detectors at the entrance of the KURAMA magnet were placed in the horizontally shifted positions to escape from the beam center. The aerogel Cherenkov counter (SAC), which was installed between SDC1 and SCH, had a hole at the beam position to suppress unwanted veto signals because of the beam interaction. The index of SAC was 1.10

and used to reject scattered π^+ at a trigger level. In contrast, trajectories of the scattered and beam particles overlapped at the downstream of the KURAMA magnet. Therefore, for each downstream detector we made a masked area at the beam region. The wires of SDC2 and SDC3 at the beam region were made insensitive by not applying the operation voltage to the potential wires. Both SDC2 and SDC3 lost about 10% and 5% of their effective area in the horizontal and vertical directions, respectively. To recover the efficiency at the insensitive areas, fine segmented hodoscopes (FHT1 and FHT2) were used as additional tracking detectors. They recovered almost all horizontal insensitive areas of SDC2 and SDC3. Beam particles penetrated 6 of 24 segments of TOF. The vertical position of beam particles was localized at the vertical center at the TOF segment. Therefore, we prepared special TOF segments, which comprised an acrylic bar, at the vertical center sandwiched between two plastic scintillators from up and down. Then, unwanted triggers caused by the beam interaction at TOF were suppressed by ensuring sufficient acceptance for scattered particles.

Charged particles involved in the Σ^+p scattering such as the recoil proton and the decay products of Σ^+ were detected using CATCH. CATCH comprises CFT, BGO, and PiID. The length of CFT along the beam axis was 400 mm. CFT comprised eight cylindrical layers of scintillation fibers with a configuration of $u1, \phi1, v2, \phi2, u3, \phi3, v4,$ and $\phi4$ outward from the center in which the fibers were arranged on each layer's cylinder surface. Each layer was coaxially placed from 49 to 84 mm in radius with a 5-mm interval in between these layers. In the four ϕ layers, fibers were placed parallel to the beam axis. In the four uv layers, fibers were arranged in a spiral shape (See [38]). This configuration enables us to three-dimensionally reconstruct the trajectories of the charged particles. The BGO calorimeter was placed around CFT and designed to measure the kinetic energy of the recoil proton from the Σ^+p scattering by stopping it in the calorimeter. The size of each BGO crystal was 400 mm(l) \times 30 mm(w) \times 25 mm(t). PiID was placed outside BGO to determine whether the charged particle penetrated BGO or not.

The (π^+, K^+) events were selected by the first- and second-level triggers. The first-level πK trigger was expressed as

$$\text{BH2} \times \text{TOF} \times \overline{\text{SAC}} \times \overline{\text{TOF}_{\text{largedE}}} \times \overline{2\text{DMtx}} \times 3\text{DMtx}, \quad (2)$$

where $\text{TOF}_{\text{largedE}}$ is a veto signal using the pulse height of TOF. It could reject particles with small β , that is, mainly protons with low momenta. 2DMtx and 3DMtx represent two types of matrix triggers, in which combinations of hit segments of SCH, TOF, and one plane of SFT were used to decide trigger. With the 2DMtx veto signal using SCH and TOF, π^+ beam events were rejected. On the other hand, the K^+ -like events were selected with the 3DMtx signal. Because the momenta of the scattered K^+ were strongly correlated with

the hit segment combinations, the matrix trigger was quite effective to suppress the trigger rate. In addition to momentum information from the hit segment combinations, selecting the range of ToF of the scattered particle enables us to identify K^+ more correctly. This is a principle of the second-level trigger, which is called “mass trigger.” The ToF gate of the mass trigger was optimized for each combination of SCH and TOF, which was accepted by 3DMtx. These matrix and mass trigger systems maintained the DAQ efficiency at 82% on an average even under the high intensity beam of $2 \times 10^7/\text{spill}$, resulting in an accepted trigger rate of around 8500/spill.

The experiment was performed in April 2019 and May-June 2020. In each period, we collected the Σ^+p scattering data for about 10 days of beam time. The pp scattering data using the proton beam with various momenta from 0.45 to 0.85 GeV/ c were collected. The pp scattering data were used for the energy calibration and estimation of the detection efficiency of CATCH.

3 Analysis I: Spectrometers and CATCH

3.1 Spectrometers for the $\pi^+p \rightarrow K^+\Sigma^+$ reaction

The Σ^+ particles were identified from the missing mass spectrum of the $\pi^+p \rightarrow K^+X$ reaction. The particle identification and momentum reconstruction for both π^+ beam and outgoing K^+ were performed using the K1.8 beam line and KURAMA spectrometers, respectively. The momenta of the produced Σ^+ particles were obtained from the momenta of π^+ and K^+ and the vertex of the $\pi^+p \rightarrow K^+X$ reaction was also reconstructed.

3.1.1 π^+ analysis

The momenta of incoming π^+ particles were analyzed by the K1.8 beam line spectrometer with the third-order transfer matrix method. Using the i -th order inverse transfer matrix $M^{(i)}$, the horizontal position at BFT x_{in} can be written with an input vector ξ as

$$x_{\text{in}} = \sum_{i=1}^5 M_{1i}^{(1)} \xi_i + \sum_{i,j} M_{1ij}^{(2)} \xi_i \xi_j + \sum_{i,j,k} M_{1ijk}^{(3)} \xi_i \xi_j \xi_k, \quad (3)$$

$$\xi = (x_{\text{out}}, u_{\text{out}}, y_{\text{out}}, v_{\text{out}}, \delta).$$

The input vector ξ comprises the horizontal position and angle, $x_{\text{out}}, u_{\text{out}}$, the vertical position and angle, $y_{\text{out}}, v_{\text{out}}$, at the down stream, and the momentum deviation from the central momentum δ of the spectrometer. x_{in} was measured with BFT and the trajectory information at the downstream, $x_{\text{out}}, u_{\text{out}}, y_{\text{out}}, v_{\text{out}}$, was reconstructed with two MWDCs (BC3 and

BC4). Equation (3) can be regarded as a cubic equation for δ , and the beam momentum is obtained as a general solution of the equation. The distribution of the reconstructed momentum of π^+ beam is shown in Fig. 2. The momentum resolution of the K1.8 beam line spectrometer $\frac{\Delta p}{p}$ is less than 1×10^{-3} in FWHM [42], although it cannot be evaluated with the experimental setup of J-PARC E40.

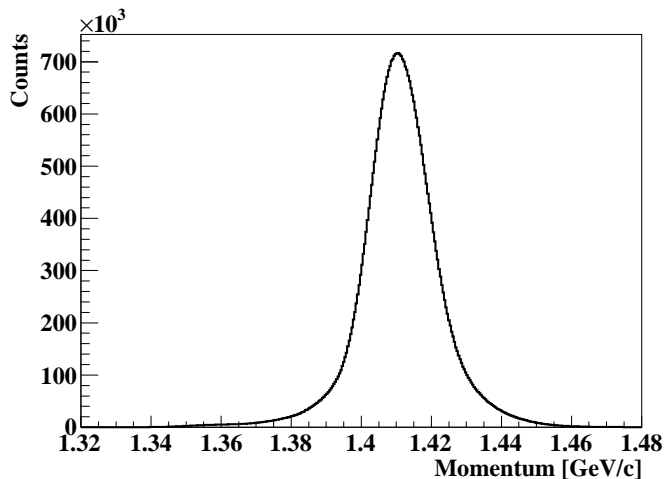


Fig. 2: Distribution of reconstructed momentum of π^+ beam obtained by the analysis of K1.8 beam line spectrometer.

3.1.2 K^+ analysis

The outgoing particles produced at the LH₂ target by the π^+p reaction were analyzed using the KURAMA spectrometer. The trajectories of the outgoing particles in the magnetic field were traced using the Runge-Kutta method [41] based on the equation of motion defined by initial parameters, namely, the momentum vector and the position at the TOF. The initial parameters were optimized to reconstruct a set of hit positions measured by the tracking detectors. The velocity β of scattered particle can be calculated by the path length L_{track} of the reconstructed trajectory and the ToF between the target and TOF. The scattered K^+ was identified by calculating the mass squared m^2 of the outgoing particles as

$$m^2 = \left(\frac{p}{\beta}\right)^2 (1 - \beta^2), \quad (4)$$

$$\beta = \frac{L_{\text{track}}}{c \cdot (\text{ToF between the target and TOF})}.$$

K^+ was selected from the m^2 gate of $0.15 < m^2[\text{GeV}^2/c^4] < 0.40$, shown by the red solid lines in Fig. 3, and the momentum gate of $0.65 < p[\text{GeV}/c] < 1.05$. There were miscalculated events in the m^2 spectrum as a constant background between the π^+ and proton peaks. These background events were derived from the high intensity π^+ beam. Hits of multiple beam particles within a short time interval caused the misidentification of the hit timing at BH2. Then, the miscalculated ToF made such a constant background in the m^2 spectrum. Using the information on the energy deposit in TOF, these events were partly rejected (see [35] in detail). The contamination rate of miscalculated events was estimated to be 8.6 % for the selected K^+ events.

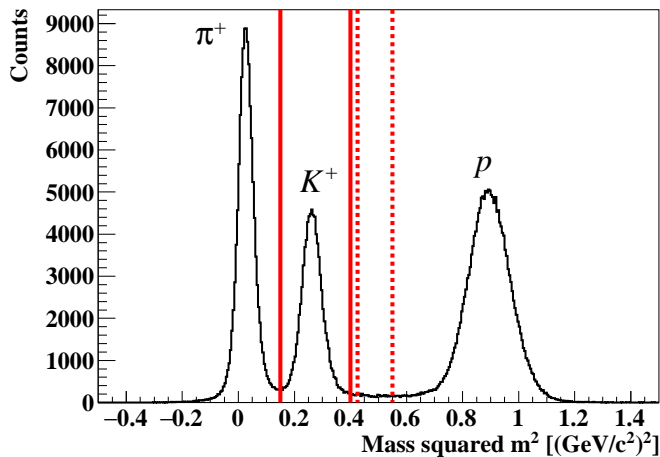


Fig. 3: Reconstructed m^2 distribution. The momentum selection ($0.65 < p[\text{GeV}/c] < 1.05$) is applied. The K^+ and side-band region is indicated by the red solid and dotted lines, respectively.

The momentum resolution of the KURAMA spectrometer was evaluated by analyzing the π^+p elastic scattering reaction. It was $\frac{\sigma_p}{p} = 2.5 \times 10^{-2}$ for 1.37 GeV/c π^+ . This resolution is insufficient to identify the Σ^+p scattering event. However, once K^+ was identified from m^2 , the K^+ momentum can be calculated from the scattering angle θ_{K^+} based on the two-body kinematics of the $\pi^+p \rightarrow K^+\Sigma^+$ reaction. In the analysis of the $\pi^+p \rightarrow K^+\Sigma^+$ reaction, the K^+ momentum calculated from θ_{K^+} was used. The momentum resolution for K^+ was $\frac{\sigma_p}{p} = 6.5 \times 10^{-3}$.

3.1.3 (π^+ , K^+) analysis

Σ^+ particles were identified from the missing mass spectrum of the $\pi^+p \rightarrow K^+X$ reaction using the reconstructed momenta of the π^+ beam and outgoing K^+ . As the closest point between π^+ and K^+ tracks, the vertex of the $\pi^+p \rightarrow K^+X$ reaction was determined. Fig. 4 shows the vertex distributions. Fig. 4a shows the z -vertex distribution. The LH₂ target can be identified from -200 to 150 mm from the vertex image. For the Σ^+p scattering analysis, the $-150 < z[\text{mm}] < 150$ region shown by the dotted lines in Fig. 4a was used, considering the CATCH acceptance. Fig. 4b shows the correlation between the x - and y -vertices. In this plot, events in which two protons were detected with CATCH were selected to emphasize the background events derived from the interaction between the π^+ beam and target vessel. The wider beam size for the x direction caused such background events. To suppress them, the x - and y -vertex regions were selected by the conditions: $x^2 + y^2 < 18^2$, $x < 14$ in mm unit, as shown by the red line in the Fig. 4b. The vertex resolution by the spectrometers was evaluated using multi particle events, such as the $\pi^+p \rightarrow \pi^+\pi^+\pi^-p$ reaction, by comparing the vertex from the spectrometer analysis with that obtained from the two different tracks measured by CATCH from the same reaction vertex. The z -vertex resolution depended on the scattering angle θ_{K^+} , and the typical resolutions were $\sigma_z = 16$ mm and 10 mm for $\theta_{K^+} = 10^\circ$ and 20° , respectively. The x - and y -vertex resolutions were evaluated as $\sigma_x = 2.6$ mm and $\sigma_y = 3.5$ mm, and the angular dependences were negligible. These vertex resolutions were considered in the simulation study to estimate the analysis cut efficiencies.

The missing mass M_X and missing momentum \mathbf{p}_X of the $\pi^+p \rightarrow K^+X$ reaction were, respectively, calculated as follows:

$$M_X = \sqrt{(E_\pi^{\text{tot}} + m_p - E_K^{\text{tot}})^2 - (\mathbf{p}_\pi - \mathbf{p}_K)^2}, \quad (5)$$

$$\mathbf{p}_X = \mathbf{p}_\pi - \mathbf{p}_K, \quad (6)$$

where $E_\pi^{\text{tot}} = \sqrt{m_\pi^2 + p_\pi^2}$ and $E_K^{\text{tot}} = \sqrt{m_K^2 + p_K^2}$ are the total energies² of the π^+ and K^+ , respectively. The missing mass spectrum of the $\pi^+p \rightarrow K^+X$ reaction is shown in Fig. 5. A clear peak corresponding to Σ^+ could be identified. As mentioned in the previous subsection, there were misidentification backgrounds in the K^+ selection derived from the multiple beam events. Their contribution was examined by selecting the side-band region in Fig. 3, that is $0.425 < m^2[\text{GeV}^2/c^4] < 0.55$ and $0.65 < p[\text{GeV}/c] < 1.05$. The red dotted histogram in Fig. 5 shows the missing mass spectrum for side-band contributions. We selected the Σ^+ particles

²In this study, a total energy is represented as E^{tot} . Mere E means a kinetic energy.

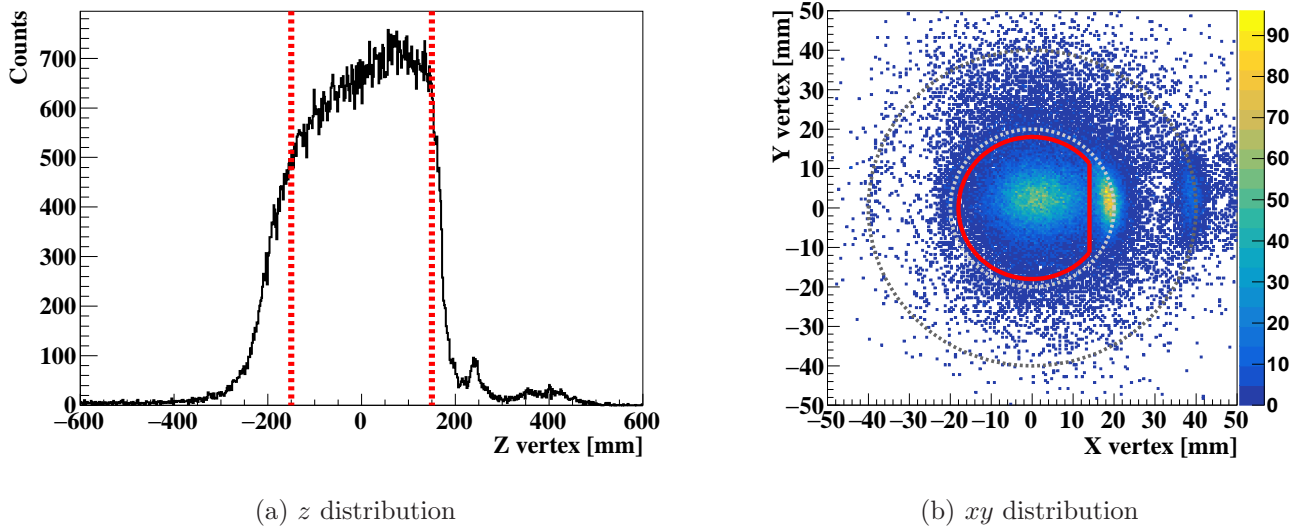


Fig. 4: Vertex distributions of the (π^+, K^+) reaction. (a) z -vertex distribution. (b) Correlation between the x - and y -vertices for events in which two protons were detected with CATCH. The gray dotted lines show the envelopes of the target container and vacuum window. The events inside the red-line region were selected to suppress the contamination of the reaction at the target container.

from 1.15 to 1.25 GeV/c^2 , as shown by the arrows in Fig.5. In total, the Σ^+ particles of 4.9×10^7 were accumulated after subtracting the contamination.

The reconstructed Σ^+ momentum as the missing momentum of the $\pi^+p \rightarrow K^+X$ reaction is shown in Fig. 6. In the Σ^+p scattering analysis, the Σ^+ beam events were categorized into three in terms of the momentum range: the low ($p_\Sigma[\text{GeV}/c] < 0.55$), middle ($0.55 < p_\Sigma[\text{GeV}/c] < 0.65$), and high ($0.65 < p_\Sigma[\text{GeV}/c] < 0.80$) momentum regions. The resolution of the Σ^+ momentum is $6 \times 10^{-3} \text{ GeV}/c$ in σ , which is mainly determined by the momentum resolution of the KURAMA spectrometer.

3.2 CATCH for recoil/decay protons

The recoil proton from the Σ^+p scattering and other charged particles, mainly decay products of Σ^+ , were detected using CATCH. CATCH mainly comprises CFT and BGO. The trajectory of the charged particle was reconstructed by CFT, and the energy deposits in CFT and BGO on the trajectory, dE_{CFT} and E_{BGO} , were summed up. The angular resolution for the tracking with CFT and the energy resolution for 100 MeV proton were evaluated to be 1.5 degrees and 6 MeV, respectively.

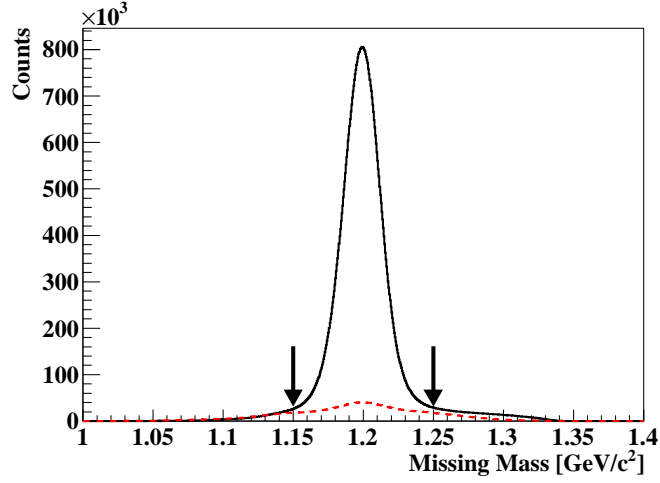


Fig. 5: Missing mass spectrum of the $\pi^+p \rightarrow K^+X$ reaction for the K^+ events (black solid line) and side-band events of K^+ (red dotted line) to estimate the effect of the contamination of the miscalculated events under the K^+ region in m^2 spectrum. Σ^+ events are selected by $1.15 < M_X[\text{GeV}/c^2] < 1.25$ gate represented by the arrows.

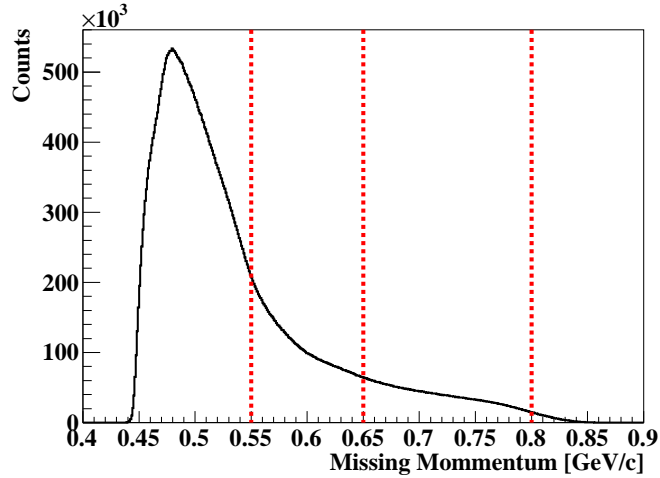


Fig. 6: Σ^+ momentum reconstructed as the missing momentum of the $\pi^+p \rightarrow K^+\Sigma^+$ reaction. The red dotted lines show the boundaries of the three momentum regions: the low ($p_\Sigma[\text{GeV}/c] < 0.55$), middle ($0.55 < p_\Sigma[\text{GeV}/c] < 0.65$), and high ($0.65 < p_\Sigma[\text{GeV}/c] < 0.80$) momentum regions.

The particle identification in CATCH was performed by the so called dE - E method between the energy loss in CFT and the summed energy deposit in CATCH ($E_{\text{meas}} = E_{\text{BGO}} + dE_{\text{CFT}}$) for each track. Fig. 7 shows the dE - E plot when the Σ^+ events were selected from the missing mass spectrum of the $\pi^+p \rightarrow K^+X$ reaction. There were three loci in this plot. These loci correspond to protons, π^+ s stopped in BGO and MIP particles (mainly π^+) penetrating BGO. For most of π , CATCH analysis can give information about only the direction and position of the track because CATCH could not measure the energy of a charged particle penetrating BGO. On the other hand, the four-momentum vector of the proton can be determined. The typical purity of the proton was 90%. The primary component of the backgrounds was the contribution of π with a high energy loss.

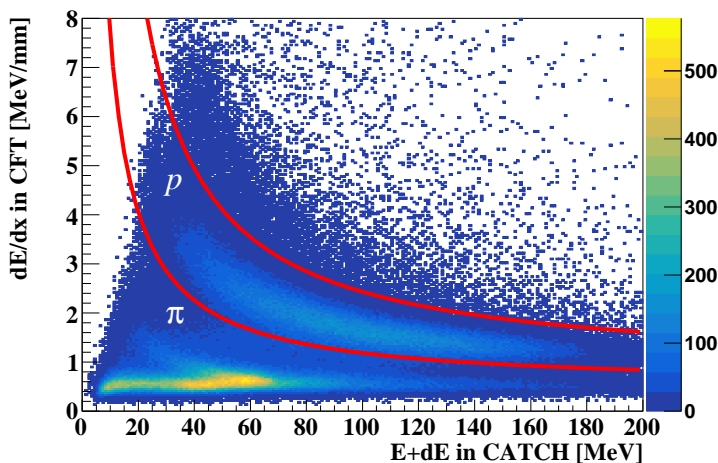


Fig. 7: dE - E correlation between the energy loss in CFT and summed energy deposit in CATCH. The two red lines show the selection region for the proton.

Particles with low kinetic energies, which were stopped in CFT, could be identified by requesting no hits for the corresponding BGO segment. Many of such particles are most likely low-energy protons. Actually, by requesting a dE/dx value of larger than 2.7 MeV/mm in CFT, such low-energy protons could be identified and were also used for the Σ^+p scattering analysis.

4 Analysis II: Analysis for the Σ^+p scattering events

As explained in the Section 3, the momentum vector of the Σ^+ beam was reconstructed from the spectrometer information and momentum vectors of the protons were determined

from the CATCH information. The combination of these information enables us to identify the Σ^+p scattering events by checking the kinematical consistency for the recoil proton between the measured energy deposit using CATCH E_{meas} and calculated kinetic energy E_{cal} . The consistency was evaluated from the difference between the two kinetic energies for the recoil proton, defined by $\Delta E = E_{\text{meas}} - E_{\text{cal}}$. The Σ^+p scattering events were identified as a peak in the ΔE spectrum. The contributions of background reactions in the ΔE histogram were estimated by a dedicated Monte Carlo simulation. By subtracting backgrounds from the ΔE spectra, the number of the Σ^+p scattering events N can be counted for each scattering angle of Σ^+ , θ_{CM} , with the angular interval of $\Delta \cos \theta_{\text{CM}} = 0.1$ and three Σ^+ momentum ranges p_{Σ} . The differential cross sections $\frac{d\sigma}{d\Omega}$ were derived by evaluating the total track length of the Σ^+ beam in the LH₂ target and efficiency for the Σ^+p scattering events, including detection efficiency.

4.1 Monte Carlo simulations

A Monte Carlo simulation was performed for many purposes. In the simulation, the dedicated event generator was implemented. By selecting the mode of the event generator, the corresponding events were generated among several implemented reactions. The implemented reactions and the purposes are as follows.

- (1) Energy calibration of CATCH: The pp and π^+p elastic scatterings were generated to obtain the relation between the proton's scattering angles and energy deposits in CFT and BGO for protons with a wide momentum range. This relation was applied to the real data for the CATCH energy calibration. The detail is described in [35][38].
- (2) The flight length evaluation of the Σ^+ beam: The flight length of Σ^+ in the LH₂ target was estimated by generating Σ^+ particles with the realistic momentum and position distribution. As the inputs of the momentum and position of Σ^+ , the analysis results of the spectrometers were used. The detail is described in Subsection 4.3.1.
- (3) Evaluation of CATCH detection efficiency for protons: Protons with arbitrary angle and energy were generated for evaluating the detection efficiency with CATCH. The detail is described in Subsection 4.3.2.
- (4) Evaluation of the overall efficiency of CATCH for the Σ^+p scattering events: The $\pi^+p \rightarrow K^+\Sigma^+$ reaction and the sequential secondary reactions in the LH₂ target were generated to evaluate the overall efficiency of CATCH. As the secondary reactions, not only the Σ^+p scattering but also background reactions that were the

reactions between the Σ^+ decay products and proton, such as the pp scattering following the $\Sigma^+ \rightarrow p\pi^0$ decay, were implemented to reproduce the background structure realistically. In this simulation, the differential cross section of the Σ^+p scattering was assumed to be 2.4 mb/sr with an isotropic angular distribution. Moreover, the secondary backgrounds were generated based on their cross sections. Further, accidental coincidence events were generated based on their measured probabilities.

The information about the generated particles by the event generator was transferred to the passage simulator based on Geant4 package [43]. In this simulator, the LH₂ target, all detectors and most materials of the KURAMA spectrometer and CATCH (the KURAMA magnet, the frames of CFT, and so on) were implemented. The interactions between the generated particles and experimental materials were simulated, and the information about the energy deposit and hit position in the virtual detectors was recorded considering the energy and position resolutions of the real detectors. The simulated records were analyzed in the same analysis program as the real data to compare between them.

4.2 Identification of the Σ^+p scattering events

In this subsection, the analysis for identifying the Σ^+p scattering events is described in detail with a comparison of the simulation study.

4.2.1 Kinematical consistency check for recoil proton (ΔE analysis)

The schematic of the Σ^+p scattering in the LH₂ target is shown in Fig. 8. The identification of the Σ^+p scattering event was performed by kinematical consistency check for the recoil proton shown by the red arrow in Fig. 8. From the kinematic relation of the Σ^+p scattering, the kinetic energy of the recoil proton E_{cal} can be calculated from the momentum of the Σ^+ beam p_Σ and the recoil angle of the recoil proton θ as

$$E_{\text{cal}} = \frac{2m_p p_\Sigma^2 \cos^2 \theta}{(E_\Sigma^{\text{tot}} + m_p)^2 - p_\Sigma^2 \cos^2 \theta}, \quad (7)$$

where $E_\Sigma^{\text{tot}} = \sqrt{p_\Sigma^2 + m_\Sigma^2}$ is the total energy of the Σ^+ beam, and m_p and m_Σ are the masses of proton and Σ^+ , respectively. The kinetic energy was also measured by CATCH, and the measured energy is denoted as E_{meas} . Then, we define the difference between the two measurements ΔE as $\Delta E = E_{\text{meas}} - E_{\text{cal}}$. If the proton really recoiled in the Σ^+p scattering, such events would make a peak around $\Delta E = 0$.

After the Σ^+p scattering, the scattered Σ^+ decays into $n\pi^+$ or $p\pi^0$. Hereafter, we focus on the Σ^+p scattering followed by the $\Sigma^+ \rightarrow p\pi^0$ decay, in which two protons can be observed

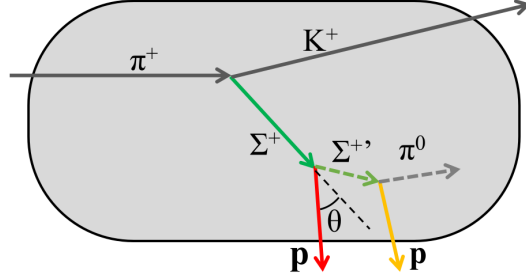


Fig. 8: Schematic of the Σ^+p scattering. In this figure, the case followed by the $\Sigma^+ \rightarrow p\pi^0$ decay is shown. θ indicates the opening angle between the Σ^+ track reconstructed with the spectrometers and the recoil proton track measured with CATCH.

with CATCH. It is because the Σ^+p scattering followed by the $\Sigma^+ \rightarrow n\pi^+$, where one proton is in the final state, are severely contaminated by the mere $\Sigma^+ \rightarrow p\pi^0$ decay and other secondary background events. Therefore, the detection of two protons with CATCH was required in the following analysis, and these events are called “two-proton events.” The ΔE spectrum for the two-proton events is shown in Fig. 9a. In analysis for the two-proton events, the proton with the smaller $|\Delta E|$ value was regarded as the recoil proton among the two protons. In Fig. 9a, a peak structure can be identified around $\Delta E = 0$ without any further selection of the Σ^+p scattering.

The ΔE spectrum was compared with the Monte Carlo simulation. As the contaminated backgrounds in the two-proton events, the four cases shown in Fig. 10 were considered in the simulation. The pp scattering following the $\Sigma^+ \rightarrow p\pi^0$ decay (a) were generated based on the cross section. In the second case (b), the $\Sigma^+ \rightarrow p\pi^0$ decay finally produces the proton and e^+e^- pair and the e^+ or e^- is misidentified as proton with CATCH by losing a large energy deposit in CFT, as mentioned in Subsection 3.2. This misidentification was reproduced by the simulation rather well. Therefore, this background contribution can be estimated by generating the Σ^+ beam event in the simulation. The other two reactions are the accidental coincidence of the Σ^+ production and different reactions for the LH₂ target (c) or target vessel (d) induced by the accidental π^+ beam. To reproduce the accidental backgrounds, the probability of accidental coincidence and distributions of the energy and angle of the accidental proton must be estimated from real data. In the real data, the π^+p elastic scattering events can be identified by detecting the recoil proton with the KURAMA spectrometer.

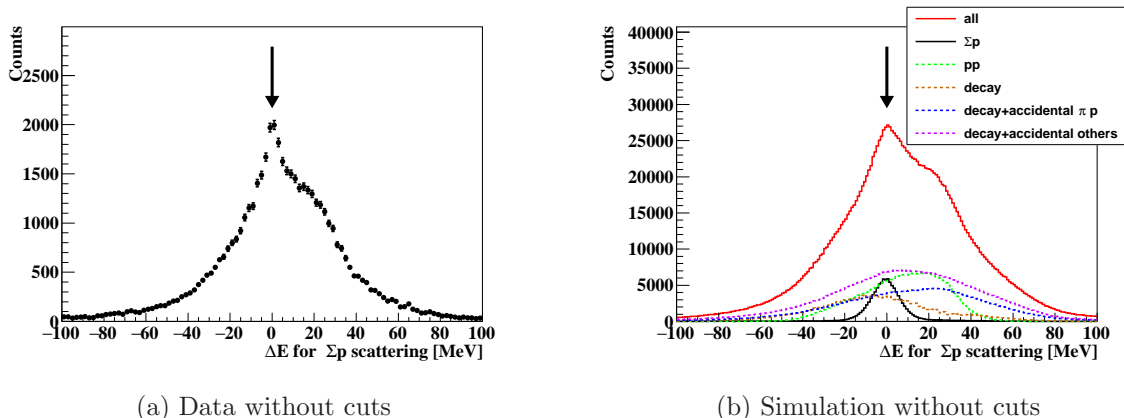


Fig. 9: ΔE spectra for the two-proton events without cuts to select the Σ^+p scattering events. As shown by the arrows, peak structure can be identified around $\Delta E = 0$. In the simulation (b), the contributions of the assumed reactions are shown reaction by reaction.

For these events, additional proton was searched for with CATCH because the additional proton was attributed to the accidental events. From this analysis, the probability for the type (c) and (d) were obtained as about 0.8% and 1.2% for the number of Σ^+ production events, respectively. These probabilities were considered in the simulation. Fig. 9b shows the ΔE spectrum obtained by analyzing the simulation considering these backgrounds. The simulated spectrum reproduced that for the real data consistently.

4.2.2 Cut conditions to select Σ^+p scattering events

To reduce the backgrounds in the ΔE spectrum shown in Fig. 9a, additional cut conditions should be considered. The information on the Σ^+ and protons was obtained from analysis for the spectrometers and CATCH, respectively. Especially, for the two-proton events, the information about momentum vectors of two protons is available for the analysis. The detailed procedures were as follows.

- (1) In the analysis for the two-proton events, the detected two protons were assigned to the recoil and decay protons depending on the ΔE value. The vertex of the Σ^+p scattering was calculated as the closest point between the Σ^+ beam and recoil proton tracks.
- (2) The momentum vector of the scattered Σ^+ , $\mathbf{p}_{\Sigma'}$, can be kinematically calculated from the recoil angle of the proton. The scattered Σ^+ is denoted as Σ' . The track of the Σ' was also determined from the vertex of the Σ^+p scattering and direction of $\mathbf{p}_{\Sigma'}$.

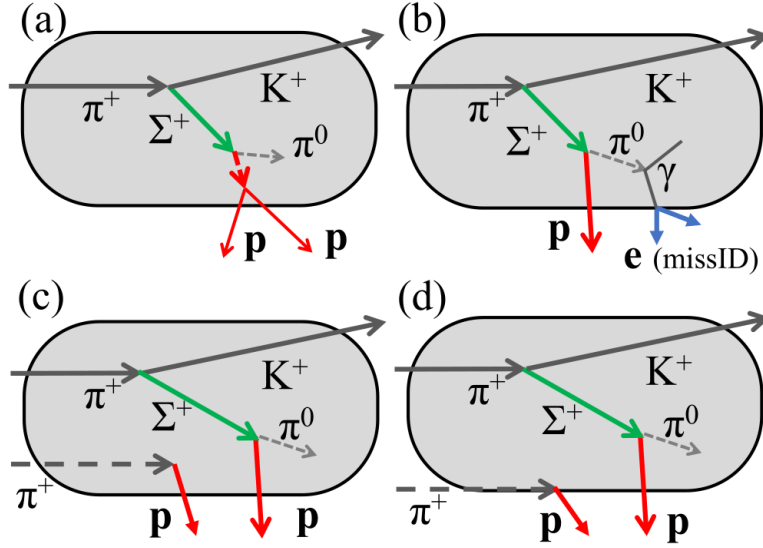


Fig. 10: Schematics of four types of backgrounds in the two-proton events. (a) the pp scattering following the $\Sigma^+ \rightarrow p\pi^0$ decay, (b) the combination of a proton from the $\Sigma^+ \rightarrow p\pi^0$ decay and the misidentified e^\pm , (c) the combination of a proton from the $\Sigma^+ \rightarrow p\pi^0$ decay and the proton from the elastic π^+p scattering in the LH_2 target caused by the accidental π^+ beam, and (d) the combination of a proton from the $\Sigma^+ \rightarrow p\pi^0$ decay and the proton from the scattering between the accidental π^+ beam and the target vessel.

- (3) The vertex of the $\Sigma' \rightarrow p\pi^0$ decay was determined as the closest point between Σ' and decay proton tracks. The missing mass for the $\Sigma' \rightarrow pX$ reaction was also calculated.

In these procedures, the two vertices, two closest distances at the two vertices, and missing mass for the $\Sigma' \rightarrow pX$ reaction were obtained. The Σ^+p scattering events were selected by applying cuts for these variables. The scattering vertex $(x_{\text{scat}}, y_{\text{scat}}, z_{\text{scat}})$ was required to be $x_{\text{scat}}^2 + y_{\text{scat}}^2 < 25^2, |z_{\text{scat}}| < 170$ in mm unit. Similarly, the decay vertex $(x_{\text{decay}}, y_{\text{decay}}, z_{\text{decay}})$ was required to be $-30 < x_{\text{decay}} < 25, |y_{\text{decay}}| < 30, |z_{\text{decay}}| < 180$ in mm unit. The closest distances at the scattering and decay points were required to be less than 20 and 25 mm, respectively. The missing mass of the $\Sigma' \rightarrow pX$ reaction M_X was required to be $M_X^2 [\text{GeV}^2/c^4] > 0$ to select the π^0 mass region.

Even after applying the cuts, the backgrounds due to the secondary pp scattering (Fig.10(a)) and the accidental π^+p elastic scattering (Fig. 10(c)) still contaminated the Σ^+p scattering events. However, the events could be suppressed by identifying the backgrounds from corresponding kinematical conditions. Because the momentum vectors of the

two protons were measured, the pp scattering events were reconstructed from the kinematical condition of the two protons and the opening angle between the two protons. The detailed analysis to identify the pp scattering is described in Appendix A. The important indices to identify the pp scattering is the difference between the measured and calculated proton momentum from the pp scattering angle, which is denoted as Δp . The Δp spectrum is shown in Fig. A2b in Appendix A. Similarly, the π^+p elastic scattering by the 1.41-GeV/ c π^+ beam shows the strong correlation between the scattering angle and kinetic energy of the recoil proton. Then, the identified pp and π^+p scattering events were removed.

The ΔE spectra for the two-proton events after applying all cuts are shown in Fig. 11. The peak structure became much clearer with the significant improvement of the signal-to-noise (S/N) ratio in $-20 < \Delta E[\text{MeV}] < 20$ region to 1.78 from 0.13 before applying the cuts shown in Fig. 9a. Here, S/N ratio was estimated by the simulation and the real data. The detailed explanation will be given in the next subsection. The simulation spectrum after the same cuts agrees with the data (Fig. 11b). The analysis efficiency for the Σ^+p scattering events are estimated to be 54.5%, and the rejection ratios of the background events are more than 90% (Table 3).

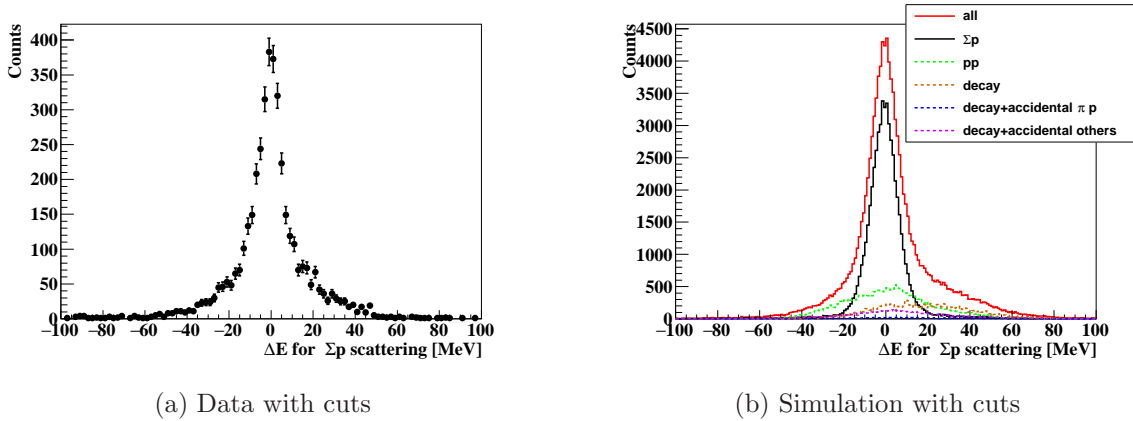


Fig. 11: ΔE spectra for the two-proton events with cuts to select the Σ^+p scattering events. In the simulation (b), the contributions of the assumed reactions are shown reaction-by-reaction.

4.2.3 Estimation of backgrounds and the number of the Σ^+p scattering events

To estimate the number of the Σ^+p scattering events and survival background events, the ΔE spectra for the Σ^+p scattering and the Δp spectra for the pp scattering following $\Sigma^+p \rightarrow p\pi^0$ decay (shown in Fig. A2b in Appendix A) were fitted with the sum of the

Table 3: Analysis efficiency (ana. eff.) of the Σ^+p scattering events and the rejection ratios (R.R) of the background events. (a)-(d) type corresponds to the background type in Fig. 10.

ana. eff. of Σ^+p	R.R of (a)-type	R.R of (b)-type	R.R of (c)-type	R.R of (d)-type
54.5 %	92.8 %	94.5 %	99.6 %	98.4 %

simulated spectra for the Σ^+p scattering and above background reactions. To reproduce the angular dependence of the background contribution correctly, the fitting was performed independently for each scattering angle of Σ^+ in the CM system with the angular interval $\Delta \cos \theta_{\text{CM}} = 0.1$, as shown in Fig. C1, C2, and C3 in Appendix C. The fitting parameters were scale factors of each reaction, and the maximum-log likelihood method was used. To constraint the scale parameter for the pp scattering background reasonably, it is necessary to fit both the ΔE spectrum for the Σ^+p scattering and the Δp spectrum for the pp scattering simultaneously. Then, the underestimation of the Σ^+p scattering events due to the overestimation of the background can be avoided. For the Δp spectra to fit, two patterns of cut conditions were examined. The first was almost the same cut condition as the ΔE for the Σ^+p scattering except for the kinematical cuts for pp scattering, that is the Δp and α cuts described in Appendix A. The second was the cut condition to emphasize the pp scattering the same as Fig. A2b. The difference of the number of the estimated Σ^+p scattering events between the fitting results was considered as the systematic uncertainty.

The ΔE and Δp spectra together with the fitted spectra for low momentum region are shown in Fig. C1 and Fig. C4 in Appendix C, respectively, for the scattering angles within the detector acceptance. For the forward angular region, the kinetic energy of the recoil proton from the Σ^+p scattering was too small to be detected. The limited acceptance for the recoil proton caused a severe deterioration in the S/N ratio of the ΔE spectra. Therefore, we set the maximum scattering angles for each Σ^+ beam momentum region. The obtained numbers of the Σ^+p scattering events are shown in Fig. 12 as a function of $\cos \theta_{\text{CM}}$ for each Σ^+ beam momentum region. The error bars and boxes represent the statistical and systematic errors. The systematic error originates in the uncertainty of the background estimation discussed in the previous paragraph. In total, about 2400 Σ^+p scattering events were identified. Fig. 13 shows the ΔE spectrum with the contributions of the involved reactions estimated from the fitting for all angular and Σ^+ beam momentum regions. The S/N ratio was estimated to be 1.78 as the ratio of the estimated signal and backgrounds in $-20 < \Delta E[\text{MeV}] < 20$ region.

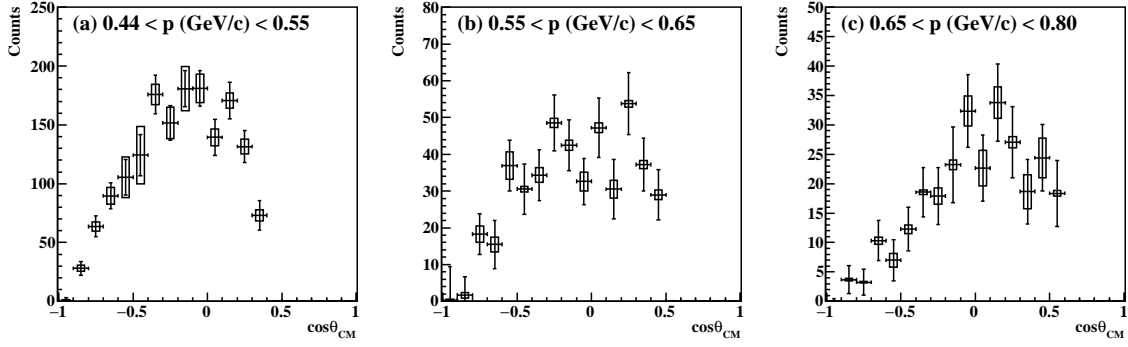


Fig. 12: The numbers of the estimated Σ^+p scattering events for each scattering angle and momentum region of Σ^+ : (a) the low momentum region ($p_\Sigma[\text{GeV}/c] < 0.55$), (b) the middle momentum region ($0.55 < p_\Sigma[\text{GeV}/c] < 0.65$), and (c) the high momentum region ($0.65 < p_\Sigma[\text{GeV}/c] < 0.80$). The error bars and boxes indicate the statistical and systematic errors, respectively.

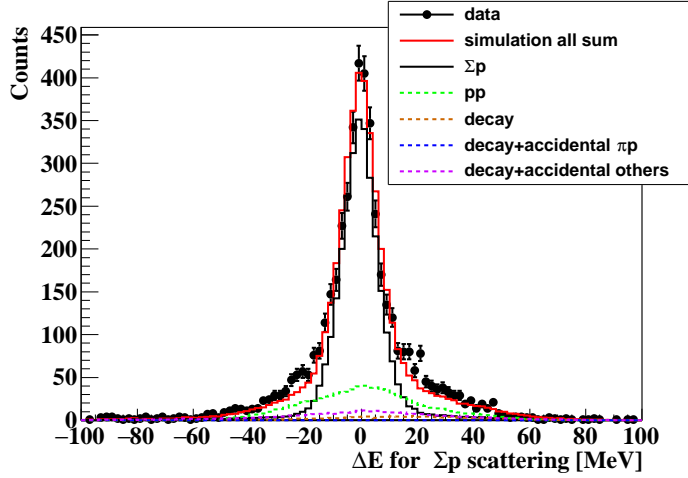


Fig. 13: ΔE spectrum for the two-proton events with the contributions of the involved reactions estimated from the fitting for all angular and Σ^+ beam momentum regions.

4.3 Derivation for differential cross sections

In the analysis in deriving the differential cross section, several values were derived for each scattering angle and Σ^+ momentum region. Therefore, these values are denoted as a function of p_Σ and $\cos\theta_{\text{CM}}$, such as the numbers of the scattering events $N(p_\Sigma, \cos\theta_{\text{CM}})$.

The differential cross section was calculated as

$$\frac{d\sigma}{d\Omega} = \frac{N(p_\Sigma, \cos \theta_{CM})}{\rho \cdot N_A \cdot L(p_\Sigma) \cdot \bar{\varepsilon}(p_\Sigma, \cos \theta_{CM}) \cdot \Delta\Omega}, \quad (8)$$

where ρ and N_A represent the density of LH₂ target, 0.071 g/cm³, and Avogadro's number, respectively. $L(p_\Sigma)$ is the total flight length of the Σ^+ beam in the LH₂ target. $\bar{\varepsilon}$ represents the efficiency for the Σ^+p scattering event and the averaged value for the vertex position was used. $\Delta\Omega$ represents the constant solid angle of $\Delta\Omega = 2\pi\Delta \cos \theta_{CM}$. The evaluation of each term is described in this section and differential cross sections are derived.

4.3.1 Total track length of the Σ^+ beam in the LH₂ target

In ordinary scattering experiments, the expression $\rho \cdot N_{Avo} \cdot t \cdot N_{\text{beam}}$ is used as the denominator in Equation 8, where t and N_{beam} represent the target thickness and number of beam particle, respectively. However, this evaluation is inappropriate in this experiment because the Σ^+ beam was produced in the LH₂ target and primarily decayed inside the target. The direct measurement for the Σ^+ track length event by event was also difficult due to the limited acceptance for the decay proton. However, the total track length of Σ^+ beam can be evaluated with the Monte Carlo simulation. The information about the production vertices and momentum vectors of all identified Σ^+ beam particles can be obtained by the spectrometer analysis. The Σ^+ particles with the obtained momenta were generated at the production points in the simulation. In the simulation, the flight length of the Σ^+ was summed up until the Σ^+ decayed or exited the target. Fig. 14 shows the estimated Σ^+ track length distribution. The total track lengths for each momentum region $L(p_\Sigma)$ were obtained as the integral of the histogram. The contribution of background in the Σ^+ beam identification shown in missing mass spectrum (Fig. 5) was also estimated from the side-band event in the m^2 distribution. The estimated total track lengths after the subtraction of background contribution are summarized in Table 4.

Table 4: Estimated Σ^+ total lengths for each momentum region for all Σ^+ events and the three momentum regions: the low momentum region ($p_\Sigma[\text{GeV}/c] < 0.55$), middle momentum region ($0.55 < p_\Sigma[\text{GeV}/c] < 0.65$), and high momentum region ($0.65 < p_\Sigma[\text{GeV}/c] < 0.80$).

Region	All	Low	Middle	High
All events [cm]	5.43×10^7	3.69×10^7	1.13×10^7	6.70×10^6
Sideband BG [cm]	0.51×10^7	0.27×10^7	0.12×10^7	0.86×10^6
Σ^+ [cm]	4.93×10^7	3.32×10^7	1.00×10^7	5.84×10^6

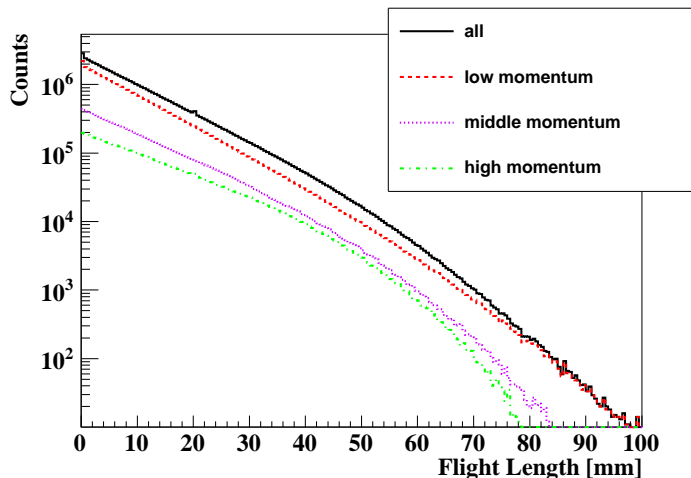


Fig. 14: Distribution of estimated Σ^+ track length for all Σ^+ events and the three momentum regions: the low momentum region ($p_\Sigma[\text{GeV}/c] < 0.55$), middle momentum region ($0.55 < p_\Sigma[\text{GeV}/c] < 0.65$), and high momentum region ($0.65 < p_\Sigma[\text{GeV}/c] < 0.80$).

In this procedure, there were uncertainties in the simulation inputs of the vertex point and momentum vector due to the resolutions and systematic errors of the spectrometer system, which might cause the uncertainties of the estimated track length. Such uncertainties were estimated to be 3% at most with the similar way as Σ^- case [35]. This uncertainty is much smaller than other uncertainties such as the statistical errors shown in Fig. 12.

4.3.2 Detection efficiency of CATCH

The detection efficiency of CATCH includes the geometrical acceptance, the tracking efficiency of the CFT, and the energy measurement efficiency for protons. They depend on the angle in the laboratory frame θ_{lab} , kinetic energy E , and position along the beam axis z . The efficiencies were evaluated based on the pp scattering data taken for the calibration purpose by irradiating the LH_2 target with proton beams of seven momenta from 0.45 to 0.85 GeV/ c . In the pp scattering, there is one-to-one correspondence between θ_{lab} and E for a fixed beam momentum. To obtain the E dependence of the efficiency for each angle θ_{lab} , several beam momenta were used for the proton beam. Thus, the efficiency was formalized as a function of θ_{lab} , E , and z based on the pp scattering data. In parallel, we estimated the proton efficiency in the Monte Carlo simulation. When the estimated efficiency agreed with the data-based efficiency, the simulated-efficiency was also used.

The procedures of the efficiency evaluation with the pp scattering data are as follows:

- (1) For the efficiency estimation, at least one proton among the two protons in the final state must be detected by CATCH. From the kinematics, the kinetic energy ($E'(\theta')$) of the detected proton with the recoil angle θ' is calculated. The scattering vertex ($x_{\text{scat}}, y_{\text{scat}}, z_{\text{scat}}$) was reconstructed as the closest point between the beam and recoil proton tracks.
- (2) The momentum vector of the other proton was expected as $\mathbf{p} = \mathbf{p}_{\text{beam}} - \mathbf{p}'_{\text{cal}}(\theta')$, where the \mathbf{p}_{beam} and \mathbf{p}'_{cal} are the proton beam momentum analyzed by the K1.8 beam-line spectrometer and the calculated momentum of the first recoil proton as discussed above, respectively. From the momentum vector \mathbf{p} , the angle and kinetic energy for the second proton can be predicted; they are denoted as θ and E , respectively.
- (3) Using the predicted proton track, the CATCH efficiency was estimated by checking the track and energy of the predicted proton are detected or not. The tracking and energy measurement efficiencies are separately derived.

First, we explain the energy measurement efficiency $\varepsilon_{\text{BGO}}(\theta, E, z_{\text{scat}})$. In this case, we checked whether the measured energy for the predicted track agreed with the predicted E within 40 MeV or not. The obtained $\varepsilon_{\text{BGO}}(\theta, E, z_{\text{scat}})$ for $\theta = 32^\circ$ is shown as the red points in Fig. 15b, as an example. This efficiency was compared with the estimated efficiency from the simulation. As shown in Fig. 15b, the simulation-based efficiency well-reproduced the data-based efficiency. Therefore, the simulation-based efficiency for the energy measurement was used for the further analysis to cover the entire θ, E , and z_{scat} regions as shown in Fig. 15a.

The tracking efficiency of CFT including the geometrical acceptance $\varepsilon_{\text{CFT}}(\theta, E, z)$ is described. The tracking efficiency $\varepsilon_{\text{CFT}}(\theta, E, z)$ was evaluated by checking whether the track with the predicted direction was detected. The energy dependence of the tracking efficiencies estimated from the pp scattering data and simulation are shown by the red and black points in Fig. 16b. Because the CFT tracking requires at least six layer's hits, the efficiency decreased rather sharply at the low energy. This energy dependence of the efficiency can be phenomenologically represented by the Fermi function for both data and simulation. Then, the efficiency was formulated as

$$\varepsilon_{\text{CFT}}(\theta, E, z) = \frac{\varepsilon_{\text{max}}(\theta, z)}{1 + e^{d(\theta)(E - E_{\text{half}}(\theta))}}, \quad (9)$$

where the $\varepsilon_{\text{max}}(\theta, z)$, $d(\theta)$ and $E_{\text{half}}(\theta)$ are the parameters to represent the maximum efficiency, diffusion, and the kinetic energy with half efficiency, respectively. These parameters were determined by fitting to efficiency evaluated with data, as shown by the red solid line in Fig. 16b. The ε_{max} of the realistic efficiency was slightly lower than that of the simulation, typically 90%. This difference is attributed to a gap between fibers in the CFT. The

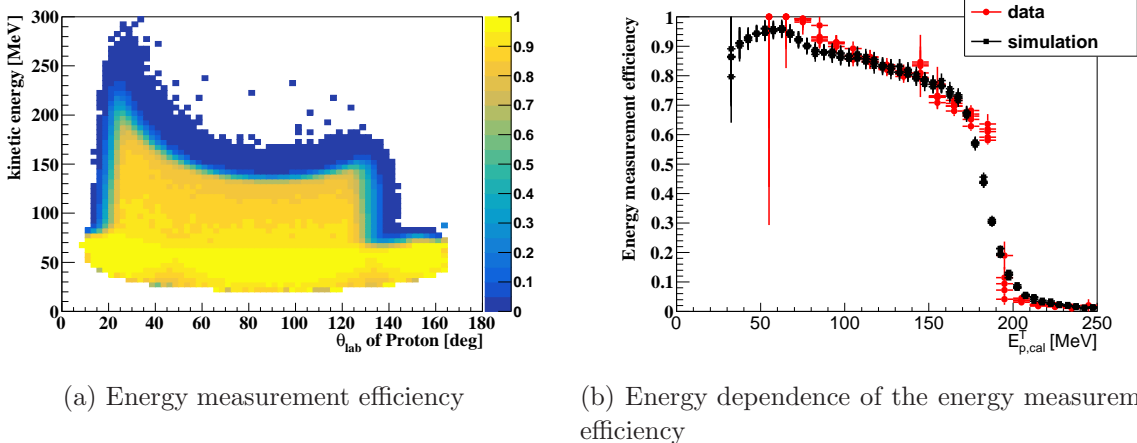
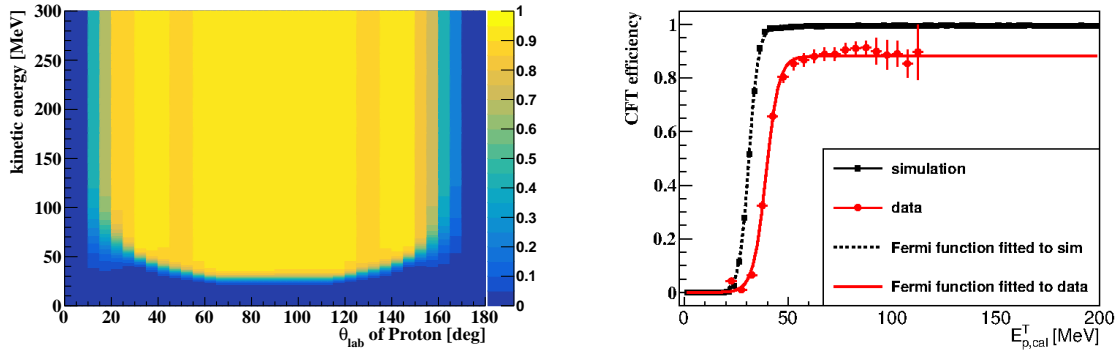


Fig. 15: (a) Typical energy measurement efficiency map evaluated by the simulation. (b) Energy dependence of the energy measurement efficiency for the scattering angle $\theta_{\text{lab}} = 32^\circ$. The red circles and black squares represent the data and simulation, respectively. The efficiencies for the various z position are written. The simulated efficiency well-reproduced data.

absolute value of the diffusion parameter d was smaller, and the kinetic energy with half efficiency E_{half} was larger than the simulated efficiency. This difference indicated that the realistic amount of material in the experimental setup was larger than that considered in the simulation. Therefore, the data-based efficiency for the CFT tracking was used for the analysis of the cross section. Fig. 16a shows the efficiency map as a function of θ and E .

The obtained efficiency maps were checked by deriving the differential cross sections of the pp scattering with proton beam for the calibration purpose. They agreed with the reference within 5%, except for the very forward angle region and low energy region, where accuracies were worse than dozens of percentages. To estimate the effect of the uncertainty of the efficiency at the acceptance edge for the Σ^+p scattering analysis, the possible lowest and highest CFT tracking efficiencies were also made by changing the parameters within a reasonable range, that is d within 20% and E_{half} within 4 MeV. The validity of the margin of the efficiency defined by the lowest and highest cases is also checked by another calibration reaction. This calibration reaction was the pp scattering following the $\Sigma^+ \rightarrow p\pi^0$ decay, which was described as the background events for the Σ^+p scattering up to now. From the data analysis, the angular distribution of the recoil proton was obtained as the red points in Fig. A3 in Appendix A. This angular distribution was also checked by the Monte Carlo simulation where this secondary pp scattering was generated with the realistic angular



(a) Tracking efficiency including the geometrical acceptance (b) Energy dependence of the tracking efficiency

Fig. 16: (a) Typical tracking efficiency map used for analysis. (b) Energy dependence of the tracking efficiency for the the scattering angle $\theta_{\text{lab}} = 54^\circ$. The red circles and black squares represent the data and simulation, respectively. The red and black curves are fitted Fermi functions for data and simulation.

distribution. In analyzing the simulation, the data-based CFT tracking efficiencies for the lowest and highest cases were considered. Then, we confirmed that the angular distribution in data was sandwiched with the two efficiency-corrected simulations, as shown by the green and blue points in Fig. A3, for the highest and lowest efficiency cases, respectively. In the next subsection, the detection efficiency for the Σ^+p scattering was corrected using these two efficiencies and the difference was considered as the systematic uncertainty.

4.3.3 Averaged efficiency for the Σ^+p scattering events including the detection and analysis efficiency

The averaged efficiency $\bar{\varepsilon}$ for the Σ^+p scattering events, including the detection and analysis efficiencies, was evaluated by analyzing the simulation with the same analyzer program for the real data. The $\bar{\varepsilon}$ is defined as

$$\bar{\varepsilon}(p_\Sigma, \cos \theta_{\text{CM}}) = \frac{N_{\text{analyzed}}(p_\Sigma, \cos \theta_{\text{CM}})}{N_{\text{generated}, \Sigma^+ \text{id}}(p_\Sigma, \cos \theta_{\text{CM}})} \quad (10)$$

$$\begin{aligned} &= \frac{N_{\text{detected}}(p_\Sigma, \cos \theta_{\text{CM}})}{N_{\text{generated}, \Sigma^+ \text{id}}(p_\Sigma, \cos \theta_{\text{CM}})} \cdot \frac{N_{\text{analyzed}}(p_\Sigma, \cos \theta_{\text{CM}})}{N_{\text{detected}}(p_\Sigma, \cos \theta_{\text{CM}})} \\ &= \bar{\varepsilon}_{\text{detect}}(p_\Sigma, \cos \theta_{\text{CM}}) \cdot \bar{\varepsilon}_{\text{ana}}(p_\Sigma, \cos \theta_{\text{CM}}). \end{aligned} \quad (11)$$

$N_{\text{generated}, \Sigma^+ \text{id}}$ in Equation (10) represents the number of generated Σ^+p scattering events in the simulation. The Σ^+ identification from the missing mass analysis in the analyzer

program is required. N_{analyzed} represents the number of identified Σ^+p scattering events, which satisfy all cut conditions for the Σ^+p scattering for the two-proton events. The effect of the branching ratio of the $\Sigma^+ \rightarrow p\pi^0$ decay is included in N_{analyzed} . The $\bar{\varepsilon}$ is transformed to the product of the detection efficiency in CATCH $\varepsilon_{\text{detect}}$ and analysis cut efficiency ε_{ana} from the second equation. N_{detected} represents the number of events where the two protons are detected with CATCH for the tagged Σ^+ events. The difference of the CFT tracking efficiency between the data $\varepsilon_{\text{CFT}}^{\text{data}}$ and simulation $\varepsilon_{\text{CFT}}^{\text{sim}}$ was corrected by changing $\bar{\varepsilon}_{\text{detect}}$ as

$$\bar{\varepsilon}_{\text{detect}} \mapsto \frac{1}{N_{\text{generated}, \Sigma^+ \text{id}}} \left(\sum_{\text{events}}^{N_{\text{detected}}} \frac{\varepsilon_{\text{CFT}}^{\text{data}}(\theta_{p_1}, E_{\text{cal}, p_1}, z_{\text{scat}}) \cdot \varepsilon_{\text{CFT}}^{\text{data}}(\theta_{p_2}, E_{\text{cal}, p_2}, z_{\text{decay}})}{\varepsilon_{\text{CFT}}^{\text{sim}}(\theta_{p_1}, E_{\text{cal}, p_1}, z_{\text{scat}}) \cdot \varepsilon_{\text{CFT}}^{\text{sim}}(\theta_{p_2}, E_{\text{cal}, p_2}, z_{\text{decay}})} \right), \quad (12)$$

where the efficiency correction for both protons are considered. The explanation of the analysis cuts is described in Subsection 4.2.2; the analysis efficiency for the entire angular region is summarized in Table 3. Here, the analysis efficiency was estimated for each angular region. The obtained efficiencies are shown in Fig. 17. The size of the vertical error represents the difference of the two possible lowest and highest CFT tracking efficiencies, as mentioned in the previous subsection. The errors for the low momentum region become relatively large because this uncertainty becomes large for the low energy proton around the edge of the energy acceptance in the CFT tracking efficiency. The angular dependence of the efficiency can be understood from the kinetic energies of the protons. The efficiency decreases for the forward scattering angle because the tracking efficiency also decreases for the recoil proton with a lower kinetic energy. Moreover, the kinetic energy of the decay proton decreases for the backward angle and the efficiency decreases for the backward angle. The errors of the efficiencies were considered as the systematic error in the derivation of the differential cross sections.

4.3.4 Differential cross sections

The differential cross section was calculated by Equation (8). The obtained differential cross sections for the three Σ^+ beam-momentum regions are shown as the black circles in Fig. 18. The mean momenta of the three-momentum regions are 0.50, 0.59, and 0.71 GeV/ c . The error bars and boxes of the data points represent the statistical and systematic uncertainties, respectively. The systematic error is estimated to be a quadratic sum of the error from the background estimation, averaged efficiency, and Σ^+ total flight length. The values of the differential cross sections and their uncertainties are summarized in Tables D1, D2, and D3 in Appendix D. For the lower two-momentum regions, past measurements at KEK, KEK E251 [33] and KEK E289 [32], are also plotted in Fig. 18 as the red boxes and blue triangles. The data quality in the present experiment is improved drastically. Now, a

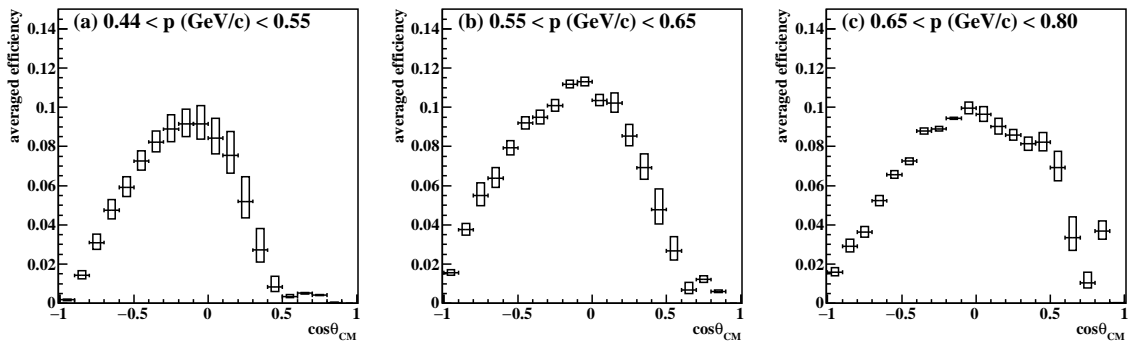


Fig. 17: Averaged efficiency for the Σ^+p scattering for each scattering angle and momentum region of Σ^+ : (a) the low momentum region ($p_\Sigma[\text{GeV}/c] < 0.55$), (b) the middle momentum region ($0.55 < p_\Sigma[\text{GeV}/c] < 0.65$), and (c) the high momentum region ($0.65 < p_\Sigma[\text{GeV}/c] < 0.80$). The size of the vertical error represents the difference in the obtained efficiency using the two possible lowest and highest CFT tracking efficiencies.

meaningful comparison with theories becomes possible. The angular dependences are rather isotropic for the present angular regions, especially for the low momentum. Moreover, the obtained values of the differential cross sections are not so large as predicted by the fss2 and FSS based on the QCM in the short-range region [6], as discussed in the next section.

5 Discussion

5.1 Comparison with theoretical calculations

The obtained data are compared with theoretical calculations, which are overlaid as lines in Fig. 18.

The blue dotted and dot-dashed lines show the calculations by FSS and fss2, which includes QCM in the short-range region [6]. Verification of the predicted large repulsive force, originating in the quark Pauli effect, is an important motivation for this experiment. The difference in the strength of the quark Pauli effect in the two models is attributed to the size parameter, which defines the size of the quark cluster in baryons. The FSS, using the larger size parameter, predicts a much repulsive interaction, which makes the differential cross section larger. However, the calculated differential cross sections by FSS and fss2 are larger than the present data, indicating that the repulsive force in QCM is too large and is unrealistic.

The green-solid and black-dashed lines show the calculations by the Nijmegen NSC97f [8] and ESC08 [15] models, respectively, based on the boson-exchange picture. Historically, in the

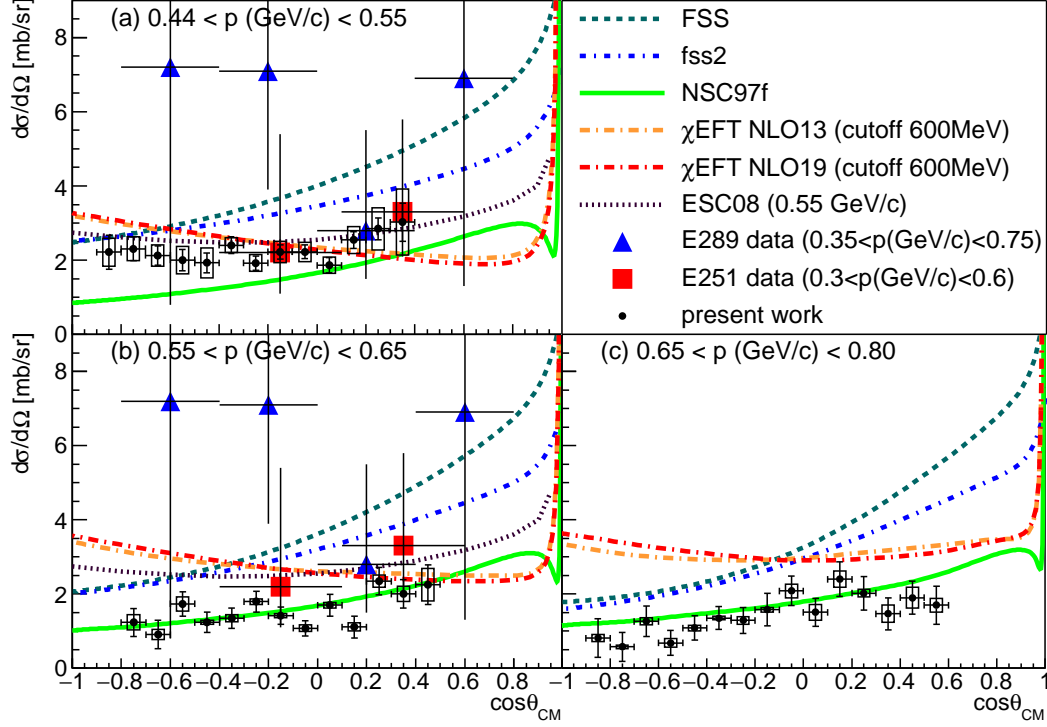


Fig. 18: Derived differential cross sections of the Σ^+p scattering for the three momentum regions: (a) the low momentum region ($p_\Sigma[\text{GeV}/c] < 0.55$), (b) the middle momentum region ($0.55 < p_\Sigma[\text{GeV}/c] < 0.65$), and (c) the high momentum region ($0.65 < p_\Sigma[\text{GeV}/c] < 0.80$). The error bars and boxes show the statistical and systematic uncertainties, respectively. The red boxes and blue triangles represent the data of past measurements, KEK E251 [33] and KEK E289 [32], respectively. The blue dotted and dot-dashed lines show the calculations by FSS and fss2 [6], respectively. The green-solid lines and black-dashed lines show the calculations by the Nijmegen NSC97f [8] and ESC08 [15] models, respectively. The orange and red dot-dashed lines show the calculations by the χ EFT NLO models [19] [20].

Nijmegen models, there have been difficulties to describe the repulsive nature in the $\Sigma N(I = 3/2, ^3S_1)$ channel. Although NSC97f agrees well with our data in terms of the differential cross sections, it predicts the attractive Σ^+p interaction, which does not agree with the current common understanding of the ΣN interaction. In ESC08, additional repulsive effects, including the quark picture, are considered by making an effective Pomeron potential as the sum of a pure Pomeron exchange and a Pomeron-like representation of the Pauli repulsion. Then, ESC08 predicts the moderate repulsive force in this channel. Although there are sizable discrepancies between the data and ESC08, especially in the middle momentum, ESC08 is

closer to the data than fss2. This suggests that the size of repulsive force used in ESC08 might be rather reasonable.

The orange and red dot-dashed lines show the calculations by the χ EFT models extended to the YN sector (NLO13 [19] and NLO19 [20], respectively) which use different sets of the LECs. In both cases, the cutoff value of 600 MeV is used. The LECs are the essential parameters of the χ EFT models, representing the short-range part of the interaction and should be determined from experimental data. At present, the LECs for S -waves are determined based on the existing hyperon-proton scattering data in the low-momentum region. Furthermore, the LECs for P -waves are not well-constrained due to the lack of experimental data, especially for the momentum region around the present data. At present, χ EFT predicts much larger cross sections especially at the higher momentum region. We expect that our data will be used to determine the LECs for P -waves in the χ EFT models.

We present the accurate data of the Σ^+p channel in the higher momentum range for the first time. At present, no theoretical model can reproduce our data consistently for the three momentum regions. This is mainly due to the lack of such accurate data. Therefore, our data become essential inputs to improve these theoretical calculations as realistic BB interaction models.

5.2 Numerical phase-shift analysis

To extract the phase shifts, especially for the 3S_1 channel, of the Σ^+p interaction from the obtained differential cross sections, a phase-shift analysis was performed. This analysis was based on only the general formulation of scattering problem in quantum mechanics. This is the first application for the hyperon-nucleon scattering data, whereas precise phase-shift analysis had been performed for the NN scattering data to derive the phase shifts for each partial wave [21]. The differential cross sections can be represented as a function of the phase shifts for 27-plet $\boldsymbol{\delta}_{[27]}$ and 10-plet $\boldsymbol{\delta}_{[10]}$, scattering angle of Σ^+ , θ_{CM} , and the momentum p_{CM} in the CM system (see Appendix B). The function is denoted as $I_0(\theta_{\text{CM}}, p_{\text{CM}}, \boldsymbol{\delta}_{[27]}, \boldsymbol{\delta}_{[10]})$, where the momentum dependence of the phase shifts should be considered. In our analysis, partial waves up to D -waves were considered. The phase shifts for the 27-plet include five channels, that is, $\boldsymbol{\delta}_{[27]} = \{\delta_{1S_0}, \delta_{3P_2}, \delta_{3P_1}, \delta_{3P_0}, \delta_{1D_2}\}$, because the 1 even and 3 odd states belong to the 27-plet. For the 10-plet, which includes 3 even and 1 odd states, five phase shifts and one mixing parameter, that is, $\boldsymbol{\delta}_{[10]} = \{\delta_{3S_1}, \delta_{1P_1}, \delta_{3D_3}, \delta_{3D_2}, \delta_{3D_1}, \epsilon_1\}$, are considered. The function $I_0(\theta_{\text{CM}}, p_{\text{CM}}, \boldsymbol{\delta}_{[27]}, \boldsymbol{\delta}_{[10]})$ has 11 phase-shift parameters. To extract meaningful information from a fitting of the differential cross sections, the number of the phase shifts to be fitted should be reduced.

The phase shifts for the 27-plet $\delta_{[27]}$ can be constrained with reliability, because in the limit of the flavor SU(3) symmetry, the $\delta_{[27]}$ become identical to the phase shifts in the $NN(I = 1,^1\text{even or }^3\text{odd})$ channel. In this case, they can be taken from the phase shifts of the pp scattering for the corresponding momentum in the CM system. In reality, the $\delta_{[27]}$ in the Σ^+p scattering should be slightly different from that in the pp scattering due to the flavor-symmetry breaking. Actually, all theories (FSS, fss2, ESC, and NSC97f) predict smaller 1S_0 phase shifts in the Σ^+p scattering than that in the pp scattering. However, the difference among the theoretical prediction of $\delta_{[27]}$ is small because these models are also constrained by the pp scattering data. In this analysis, the effect of the uncertainty in the $\delta_{[27]}$ was examined using three different sets of $\delta_{[27]}$, which are taken from results of the phase-shift analysis of the pp scattering, and theoretical predictions in ESC16 [16] and NSC97f [8].

Moreover, the remaining phase shifts for the 10-plet $\delta_{[10]}$ are unique to the $\Sigma N(I = 3/2)$ channel and these phase shifts should be determined from the fitting. However, six parameters are still too much to perform the fitting to the present data. Therefore, two theoretically uncertain phase shifts, δ_{3S_1} and δ_{1P_1} , which include the short-range interaction, were regarded as free parameters. Moreover, the variation among the theoretical models for the rest of phase shifts, namely, $\delta_{3D_3}, \delta_{3D_2}, \delta_{3D_1}$, and ϵ_1 , is rather small because the pion-exchange mechanism is expected to be dominant for the interaction range. Therefore, these values were fixed to the theoretical values as an approximation.

In summary, the two phase-shift parameters, δ_{3S_1} and δ_{1P_1} , were obtained by fitting the differential cross sections with the function $I_0(\theta_{\text{CM}}, p_{\text{CM}}, \delta_{[27]}, \delta_{[10]})$. To study the effect of the uncertainties due to the assumed fixed phase shifts on the determination of δ_{3S_1} and δ_{1P_1} , the fitting was performed for three conditions with different sets of the fixed parameters.

- A $\delta_{[27]}$ was fixed to values taken from the pp scattering. $\delta_{3D_3}, \delta_{3D_2}, \delta_{3D_1}$, and ϵ_1 were fixed to 0.
- B $\delta_{[27]}$ was fixed to values of the ESC16 or NSC97f. $\delta_{3D_3}, \delta_{3D_2}, \delta_{3D_1}$, and ϵ_1 were fixed to 0.
- C $\delta_{[27]}$ was fixed to values of the ESC16 or NSC97f. $\delta_{3D_3}, \delta_{3D_2}, \delta_{3D_1}$, and ϵ_1 were fixed to values of ESC16 or NSC97f.

From the comparison between conditions A and B, the effect of the uncertainty in the $\delta_{[27]}$ was studied. From conditions B and C, the effect of the uncertainty in the other parameters, $\delta_{3D_3}, \delta_{3D_2}, \delta_{3D_1}$, and ϵ_1 , was evaluated. Although the sign of δ_{3S_1} is expected to be negative, as predicted by recent theoretical models, including ESC16, numerical fittings with a positive δ_{3S_1} can be possible using a different set of the phase-shift parameters like NSC97f. As

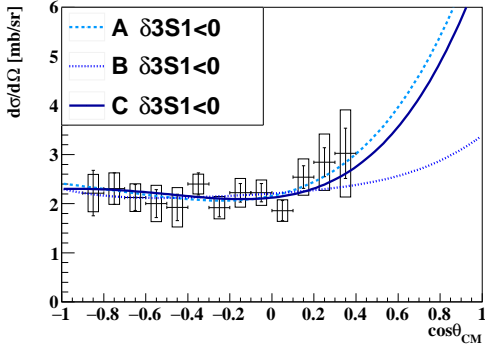
shown in condition C, the $\delta_{[10]}$ parameter sets $(\delta_{3D_3}, \delta_{3D_2}, \delta_{3D_1}, \epsilon_1)$ of ESC16 and NSC97f were used to derive the negative and positive δ_{3S_1} values, respectively. The fixed phase shifts are summarized in Table 5.

Table 5: $\delta_{[27]}$ and $\delta_{[10]}$ for the pp scattering and Σ^+p scattering in ESC16 [16] and NSC97f [8]. The units of p_Σ and p_{CM} are [GeV/ c]. E_{lab}^{pp} (unit: [MeV]) represents the kinetic energy of the beam proton in the pp scattering in which p_{CM} equals to that of the Σ^+p scattering. The units of phase shifts are degrees.

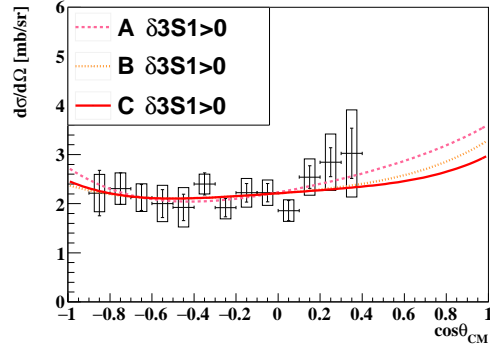
	pp	ESC16	NSC97f	pp	ESC16	NSC97f	pp	ESC16	NSC97f
	low	low	low	mid	mid	mid	high	high	high
p_Σ	0.496	0.50	0.50	0.59	0.60	0.60	0.71	0.70	0.70
p_{CM}	0.214	0.216	0.216	0.253	0.257	0.257	0.303	0.297	0.297
E_{lab}^{pp}	87.6	–	–	122.1	–	–	173.7	–	–
δ_{1S_0}	27.9	19.1	20.2	19.5	10.8	11.8	10.4	2.80	3.71
δ_{3P_2}	9.92	6.76	6.44	12.7	8.50	8.02	14.9	9.82	9.04
δ_{3P_1}	–12.2	–13.2	–13.3	–15.5	–16.9	–17.1	–19.5	–20.8	–21.0
δ_{3P_0}	10.5	7.19	8.10	7.29	3.59	4.49	2.15	–0.92	–0.23
δ_{1D_2}	3.24	3.38	3.25	4.71	4.99	5.02	6.41	6.61	6.99
δ_{3S_1}	–	(–27.9)	(21.9)	–	(–32.6)	(28.5)	–	(–36.6)	(35.01)
δ_{1P_1}	–	(8.33)	(12.2)	–	(8.45)	(13.71)	–	(7.46)	(13.7)
δ_{3D_3}	–	1.14	1.42	–	1.59	2.29	–	1.93	3.18
δ_{3D_2}	–	–3.53	–3.23	–	–4.87	–4.23	–	–6.42	–5.31
δ_{3D_1}	–	1.35	1.48	–	0.69	1.30	–	–0.70	0.41
ϵ_1	–	–5.04	–1.65	–	–5.24	0.11	–	–5.14	1.87

The fitting results for the three momentum regions are shown in Fig. 19, 20, and 21, respectively. In all momentum regions, reasonable reduced χ^2 values around one were obtained. The momentum dependence of the obtained δ_{3S_1} and δ_{1P_1} are plotted in Fig. 22. In all conditions using the different fixed parameter sets, the δ_{3S_1} values are similar with each other. Therefore, the uncertainty originating in these fixed parameters is sufficiently small for the δ_{3S_1} . The absolute values of δ_{3S_1} are about 20° to 35° for the present momentum ranges. If the sign is assumed to be negative, the momentum dependence of the δ_{3S_1} is rather consistent with the ESC models, suggesting that the repulsive force is moderate as in the ESC models, as already discussed in Subsection 5.1. Moreover, the obtained δ_{1P_1} values

deviate within $-5^\circ < \delta_{1P_1} < 25^\circ$ with each other depending on the conditions. Although the results of the δ_{1P_1} are rather ambiguous, they may support the predictions of fss2, ESC, and NSC97f in which the interaction of the 1P_1 state in the Σ^+p system is weakly attractive.

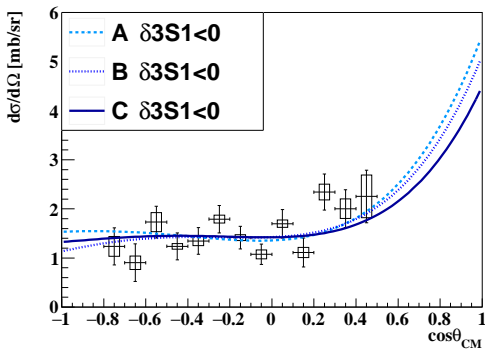


(a) $\delta_{3S_1} < 0$ case

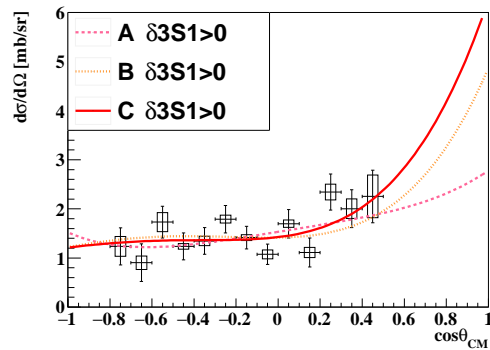


(b) $\delta_{3S_1} > 0$ case

Fig. 19: Results of the phase-shift analysis for the low momentum region ($p_\Sigma[\text{GeV}/c] < 0.55$). The typical χ^2/ndf is 4.4/11.



(a) $\delta_{3S_1} < 0$ case



(b) $\delta_{3S_1} > 0$ case

Fig. 20: Results of the phase-shift analysis for the middle momentum region ($0.55 < p_\Sigma[\text{GeV}/c] < 0.65$). The typical χ^2/ndf is 14.0/11.

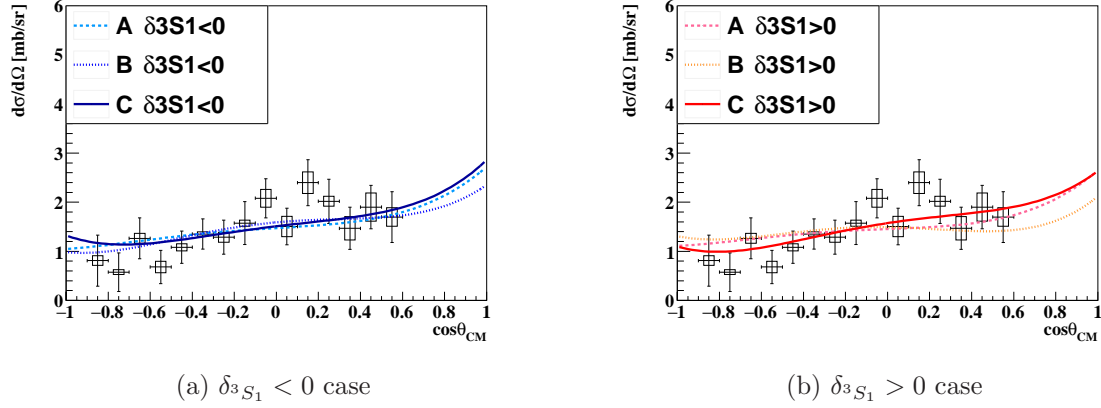


Fig. 21: Results of the phase-shift analysis for the high momentum region ($0.65 < p_\Sigma[\text{GeV}/c] < 0.80$). The typical χ^2/ndf is 11.0/13.

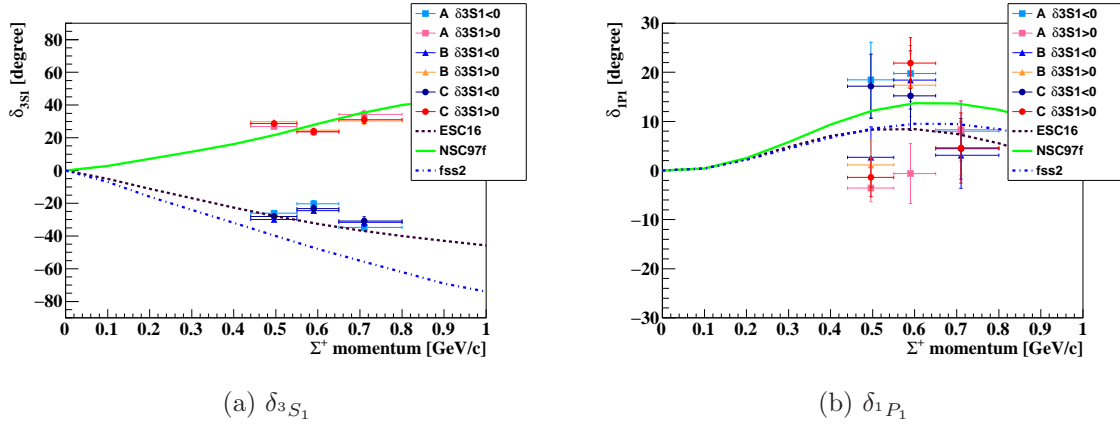


Fig. 22: Momentum dependence of the obtained phase shift δ_{3S_1} and δ_{1P_1} . The black-dashed, green-solid, blue dotted lines represent the calculated phase shifts of ESC16 [16], NSC97f [8], and fss2 [6], respectively.

6 Summary and prospects

Revealing the nature of flavor SU(3) multiplets is important for the systematic understanding of the BB interactions. Among them, the 10-plet is predicted to be considerably repulsive due to the Pauli effect in the quark level, which is closely related to the origin of the repulsive core in the nuclear force. The $\Sigma N(I = 3/2)$ channel is one of the best channels

to study the repulsive nature in the 10-plet because the $\Sigma N(I = 3/2)$ channel is simply represented by a well-estimated 27-plet in the 1 even and 3 odd channels and the 10-plet in the 3 even and 1 odd channels.

Hyperon-proton scattering experiment is one of the most direct methods to study the YN interaction, as in the case of the NN interaction. Although it was experimentally difficult due to short lifetime of hyperons for a long time, we successfully performed novel high-statistics Σp scattering experiment at J-PARC (J-PARC E40). In this experiment, we measured the differential cross sections of not only the $\Sigma^+ p$ elastic scattering but also the $\Sigma^- p$ elastic and $\Sigma^- p \rightarrow \Lambda n$ inelastic scatterings. In this study, we reported the detailed results of the $\Sigma^+ p$ elastic scattering to investigate the $\Sigma N(I = 3/2)$ interaction.

The experiment was performed at the K1.8 beam line in the J-PARC Hadron Experimental Facility in the separated periods of April 2019 and May-June 2020 for the data collection of the $\Sigma^+ p$ scattering. The π^+ beam, having a high intensity of approximately 2×10^7 /spill and the central momentum of 1.41 GeV/ c , was used to produce many Σ^+ particles inside the LH₂ target via the $\pi^+ p \rightarrow K^+ \Sigma^+$ reaction. The produced Σ^+ was momentum-tagged from the beam π^+ and outgoing K^+ , which were analyzed using the beam-line and forward spectrometers, respectively. In total, 4.9×10^7 Σ^+ were tagged and these Σ^+ , traveling inside the LH₂ target, were regarded as the Σ^+ beam. The $\Sigma^+ p$ scattering events, which were induced by the interactions between the Σ^+ beam and protons in the LH₂ target, were identified by detecting the recoil proton using the surrounding detector system CATCH. To suppress the backgrounds, detection of the proton from the $\Sigma^+ \rightarrow p\pi^0$ decay with CATCH was also required. The $\Sigma^+ p$ scattering was identified by checking the consistency for the recoil proton between the measured energy and the calculated energy from kinematics of the $\Sigma^+ p$ scattering. In total, approximately 2400 $\Sigma^+ p$ elastic scattering events were identified in the momentum range of 0.44 – 0.80 GeV/ c .

The differential cross sections of the $\Sigma^+ p$ scattering were derived for the three separated-momentum regions. Their uncertainties were typically less than 20% with an angular step of $\Delta \cos \theta_{\text{CM}} = 0.1$, and the data quality was drastically improved. The angular dependences of the obtained differential cross sections are rather isotropic for the present angular regions of $-0.8 < \cos \theta_{\text{CM}} < 0.6$, especially for the low momentum. The obtained values of the differential cross sections are around 2 mb/sr, which are not so large as predicted by the fss2 and FSS based on the QCM in the short-range region [6]. The Nijmegen ESC models [15][16], which include the moderate repulsive force by the Pomeron effect, were close to the data, although there are still sizable discrepancies between the data and ESC08. χ EFT predicts much larger cross sections, especially at the higher momentum region. We expect that our data will be used to specify the LECs for P -waves in the χ EFT models [19][20].

Owing to precise data points and the simple representation of the Σ^+p system with respect to the multiplets of the BB interaction, we derived the phase shifts of the 3S_1 and 1P_1 channels for the first time by performing the phase-shift analysis for the obtained differential cross sections. In this analysis, the less uncertain phase shifts were fixed to the theoretical values, and two important phase shifts, that is δ_{3S_1} and δ_{1P_1} , were determined by the fitting. Although such a treatment includes the uncertainties depending on the used sets of the fixed phase-shift values, the obtained δ_{3S_1} value does not depend on the selection of the fixed phase-shift sets well. The absolute values of δ_{3S_1} are about 20° to 35° for the present momentum range. If the sign is assumed to be negative, the momentum dependence of the δ_{3S_1} is rather consistent with the ESC models, suggesting that the repulsive force is moderate like ESC models, as shown in the discussion of the differential cross sections.

Finally, we provided a series of the differential cross sections of the Σp scatterings in the J-PARC E40 experiment. Together with the Σ^-p elastic scattering [35] and $\Sigma^-p \rightarrow \Lambda n$ inelastic scattering [36] data, new accurate measurements of the Σ^+p elastic scattering are presented. These systematic studies of the YN interactions will play extremely important roles for understanding the contribution of quark-quark interaction to the BB interaction. Moreover, these systematic measurements are essential inputs to improve the BB interaction models to be more realistic. We hope that realistic BB interaction models will be established with both theoretical and experimental efforts in near future.

Acknowledgment

We would like to thank the staff of the J-PARC accelerator and the Hadron Experimental Facility for their support to provide beam during the beam time. We also thank the staff of CYRIC and ELPH at Tohoku University for their support in providing beams for the test experiments for our detectors. We would like to express gratitude to Y. Fujiwara for theoretical support from the initial stages of the experimental design, such as how to extract the contribution of the 3S_1 state from the differential cross sections. We also thank T. A. Rijken and J. Haidenbauer for their theoretical calculations. We appreciate computational and network resources provided by KEKCC and SINET4. This work was supported by JSPS KAKENHI Grant Number 23684011, 15H00838, 15H05442, 15H02079 and 18H03693. This work was also supported by Grants-in-Aid Number 24105003 and 18H05403 for Scientific Research from the Ministry of Education, Culture, Science and Technology (MEXT) Japan.

References

- [1] T. Hamada and I. D. Hohnston, Nucl. Phys., **34**, 382 (1962). [https://doi.org/10.1016/0029-5582\(62\)90228-6](https://doi.org/10.1016/0029-5582(62)90228-6).

- [2] R. Machleidt, K. Holinde, and Ch. Elster, *Phys. Rep.*, **149**, 1 (1987). [https://doi.org/10.1016/S0370-1573\(87\)80002-9](https://doi.org/10.1016/S0370-1573(87)80002-9).
- [3] M. Oka and K. Shimizu, *Prog. Theor. Phys.*, **66**, 556 (1981). <https://doi.org/10.1143/PTP.66.556>.
- [4] M. Oka and K. Shimizu, *Prog. Theor. Phys.*, **66**, 572 (1981). <https://doi.org/10.1143/PTP.66.572>.
- [5] M. Oka, K. Shimizu, and K. Yazaki, *Nucl. Phys. A*, **464**, 700 (1987). [https://doi.org/10.1016/0375-9474\(87\)90371-X](https://doi.org/10.1016/0375-9474(87)90371-X).
- [6] Y. Fujiwara, Y. Suzuki, and C. Nakamoto, *Prog. Part. Nucl. Phys.*, **58**, 439 (2007). <https://doi.org/10.1016/j.pnpnp.2006.08.001>.
- [7] P. M. M. Maessen, Th. A. Rijken, and J. J. de Swart, *Phys. Rev. C*, **40**, 2226 (1989). <https://doi.org/10.1103/PhysRevC.40.2226>.
- [8] Th. A. Rijken, V. G. J. Stoks, and Y. Yamamoto, *Phys. Rev. C*, **59**, 21 (1999). <https://doi.org/10.1103/PhysRevC.59.21>.
- [9] B. Holzenkamp, K. Holinde, and J. Speth, *Nucl. Phys. A*, **500**, 485 (1989). [https://doi.org/10.1016/0375-9474\(89\)90223-6](https://doi.org/10.1016/0375-9474(89)90223-6).
- [10] T. Nagae et al., *Phys. Rev. Lett.*, **80**, 1605 (1998). <https://doi.org/10.1103/PhysRevLett.80.1605>.
- [11] H. Noumi et al., *Phys. Rev. Lett.*, **89**, 072301 (2002). <https://doi.org/10.1103/PhysRevLett.89.072301>.
- [12] P. K. Saha et al., *Phys. Rev. C*, **70**, 044613 (2004). <https://doi.org/10.1103/PhysRevC.70.044613>.
- [13] T. Harada, R. Honda, and Y. Hirabayashi, *Phys. Rev. C*, **97**, 024601 (2018). <https://doi.org/10.1103/PhysRevC.97.024601>.
- [14] R. Honda et al., *Phys. Rev. C*, **96**, 014005 (2017). <https://doi.org/10.1103/PhysRevC.96.014005>.
- [15] Th. A. Rijken, M. M. Nagels, and Y. Yamamoto, *Prog. Theor. Phys.*, **185**, 14 (2010). <https://doi.org/10.1143/PTPS.185.14>.
- [16] M. M. Nagels, Th. A. Rijken, and Y. Yamamoto, *Phys. Rev. C*, **99**, 044003 (2019). <https://doi.org/10.1103/PhysRevC.99.044003>.
- [17] T. Inoue et al., *AIP Conf. Proc.*, **2130**, 020002 (2019). <https://doi.org/10.1063/1.5118370>.
- [18] H. Nemura et al., *EPJ Web of Conf.*, **175**, 05030 (2018). <https://doi.org/10.1051/epjconf/201817505030>.
- [19] J. Haidenbauer, S. Petschauer, N. Kaiser, Ulf-G. Meißner, A. Nogga, and W. Weise, *Nucl. Phys. A*, **915**, 24 (2013). <https://doi.org/10.1016/j.nuclphysa.2013.06.008>.
- [20] J. Haidenbauer, Ulf-G. Meißner, and A. Nogga, *Eur. Phys. J. A*, **56**, 91 (2020). <https://doi.org/10.1140/epja/s10050-020-00100-4>.
- [21] A. Arndt, Igor I. Strakovsky, and Ron L. Workman, *Phys. Rev. C*, **62**, 034005 (2000). <https://doi.org/10.1103/PhysRevC.62.034005>.
- [22] I. Vida na, *Nucl. Phys. A*, **914**, 367 (2013). <https://doi.org/10.1016/j.nuclphysa.2013.01.015>.
- [23] Y. Yamamoto, T. Furumoto, N. Yasutake, and Th. A. Rijken, *Phys. Rev. C*, **90**, 045805 (2014). <https://doi.org/10.1103/PhysRevC.90.045805>.
- [24] B. Sechi-Zorn, B. Kehoe, J. Twitty, and R. A. Burnstein, *Phys. Rev.*, **175**, 1735 (1968). <https://doi.org/10.1103/PhysRev.175.1735>.
- [25] G. Alexander et al., *Phys. Rev.*, **173**, 1452 (1968). <https://doi.org/10.1103/PhysRev.173.1452>.
- [26] J. A. Kadyk, G. Alexander, J. H. Chan, P. Gaposchkin, and G. H. Trilling, *Nucl. Phys. B*, **27**, 13 (1971). [https://doi.org/10.1016/0550-3213\(71\)90076-9](https://doi.org/10.1016/0550-3213(71)90076-9).
- [27] J. M. Hauptman, J. A. Kadyk, and G. H. Trilling, *Nucl. Phys. B*, **125**, 29 (1977). [https://doi.org/10.1016/0550-3213\(77\)90222-X](https://doi.org/10.1016/0550-3213(77)90222-X).
- [28] R. Engelmann, H. Filthuth, V. Hepp, and E. Kluge, *Phys. Lett.*, **21**, 587 (1966). [https://doi.org/10.1016/0031-9163\(66\)91310-2](https://doi.org/10.1016/0031-9163(66)91310-2).
- [29] F. Eisele, H. Filthuth, W. Fölisch, V. Hepp, and G. Zech, *Phys. Lett.*, **37B**, 204 (1971). [https://doi.org/10.1016/0370-2693\(71\)90053-0](https://doi.org/10.1016/0370-2693(71)90053-0).
- [30] D. Stephen, University of Massachusetts Ph.D. thesis (1970).
- [31] Y. Kondo et al., *Nucl. Phys. A*, **676**, 371 (2000). [https://doi.org/10.1016/S0375-9474\(00\)00191-3](https://doi.org/10.1016/S0375-9474(00)00191-3).
- [32] J. K. Ahn et al., *Nucl. Phys. A*, **761**, 41 (2005). <https://doi.org/10.1016/j.nuclphysa.2005.07.004>.
- [33] J. K. Ahn et al., *Nucl. Phys. A*, **648**, 263 (1999). [https://doi.org/10.1016/S0375-9474\(99\)00028-7](https://doi.org/10.1016/S0375-9474(99)00028-7).
- [34] M. Kurosawa et al., *Jpn. J. Appl. Phys.*, **45**, 4204 (2006). <https://doi.org/10.1143/JJAP.45.4204>.
- [35] K. Miwa et al., *Phys. Rev. C*, **104**, 045204 (2021). <https://doi.org/10.1103/PhysRevC.104.045204>.
- [36] K. Miwa et al., *Phys. Rev. Lett.*, **128**, 072501 (2022). <https://doi.org/10.1103/PhysRevLett.128.072501>.
- [37] K. Agari et al., *PTEP*, **2012**, 02B009 (2012). <https://doi.org/10.1093/ptep/pts038>.
- [38] Y. Akazawa et al., *Nucl. Inst. Meth. A*, **1029**, 166430 (2022). <https://doi.org/10.1016/j.nima.2022.166430>.
- [39] R. Honda, K. Miwa, Y. Matsumoto, N. Chiga, S. Hasegawa, and K. Imai, *Nucl. Instr. Meth. A*, **787**, 157 (2015). <https://doi.org/10.1016/j.nima.2014.11.084>.
- [40] S. Morinobu, unpublished.

- [41] J. Myrheim and L. Bugge, Nucl. Inst. Meth., **160**, 43 (1979). [https://doi.org/10.1016/0029-554X\(79\)90163-0](https://doi.org/10.1016/0029-554X(79)90163-0).
- [42] T. Takahashi et al., PTEP, **2012**, 02B010 (2012). <https://doi.org/10.1093/ptep/pts023>.
- [43] Geant4 homepage(<http://geant4.web.cern.ch/>).
- [44] V. F. J. Stoks, R. A. M. Klomp, M. C. M. Rentmeester, and J. J. de Swart, Phys. Rev. C, **48**, 792 (1993). <https://doi.org/10.1103/PhysRevC.48.792>.
- [45] N. Hoshizaki, Supplement of the Progress of Theoretical Physics, **42**, 107 (1968). <https://doi.org/10.1143/PTPS.42.107>.

A Appendix A: Kinematical consistency check for the pp scattering following the $\Sigma^+ \rightarrow p\pi^0$ decay (Δp analysis)

The pp scattering following the $\Sigma^+ \rightarrow p\pi^0$ decay shown in Fig. A1 is the main background reaction in two-proton events. This reaction can be identified by the kinematical consistency check for the decay proton.

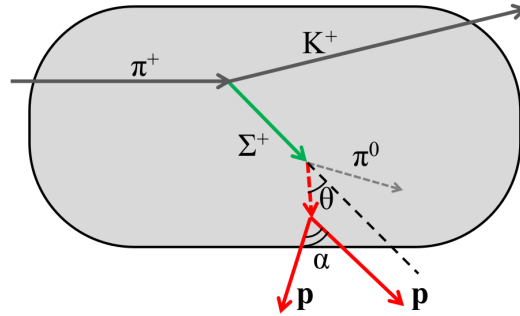


Fig. A1: Schematic of the pp scattering following the $\Sigma^+ \rightarrow p\pi^0$ decay. θ indicates the opening angle between the Σ^+ track reconstructed with spectrometers and the decay proton track. The momentum of the decay proton was reconstructed from the momenta of the two protons detected with CATCH.

The analysis for this reaction required the Σ^+ identification with spectrometers and the detection of two protons with CATCH. Assuming the two protons were derived from this reaction, the momentum of the decay proton \mathbf{p} can be reconstructed from the momenta of the two detected protons $\mathbf{p}_1, \mathbf{p}_2$ as $\mathbf{p} = \mathbf{p}_1 + \mathbf{p}_2$. The reconstructed momentum is regarded as p_{meas} . Because the scattering vertex of the pp scattering could be calculated as the closest point between the two proton tracks, the tracks of decay proton were reconstructed. The momentum of the decay proton can be calculated from the Σ^+ beam momentum p_Σ and the

opening angle between the Σ^+ and the proton tracks θ as

$$\begin{aligned}
p_{\text{decay},\text{cal}} &= \frac{Ap_{\Sigma} \cos \theta + \sqrt{D}}{E_{\Sigma}^{\text{tot}^2} - p_{\Sigma}^2 \cos^2 \theta}, \\
A &= \frac{m_{\Sigma}^2 + m_p^2 - m_{\pi^0}^2}{2}, \\
D &= (Ap_{\Sigma} \cos \theta)^2 - (E_{\Sigma}^{\text{tot}^2} - p_{\Sigma}^2 \cos^2 \theta)(m_p^2 E_{\Sigma}^{\text{tot}^2} - A^2),
\end{aligned} \tag{A1}$$

where $E_{\Sigma}^{\text{tot}} = \sqrt{p_{\Sigma}^2 + m_{\Sigma}^2}$ is the total energy of the Σ^+ beam, and m_p, m_{Σ} , and m_{π^0} are the masses of proton, Σ^+ , and π^0 , respectively. If the events were really originated from this reaction, $\Delta p = p_{\text{meas}} - p_{\text{decay},\text{cal}}$ distribute around 0. The opening angle of two detected proton α can also be used to identify the pp scattering, which are distributed at around 90° . The correlation of the Δp and α is shown in Fig. A2a. As the cut condition to select the Σ^+p scattering events, events in $82^\circ < \alpha < 92^\circ$ and $-0.065 < \Delta p[\text{GeV}/c] < 0.035$, that is $\pm 2\sigma$ of the pp scattering peak, were rejected. On the other hand, $79^\circ < \alpha < 95^\circ$ and $-0.090 < \Delta p < 0.060$ regions were selected when we focus on this reaction. The Δp spectrum is shown in Fig. A2b, where the selection of scattering vertex $(x_{\text{scat}}, y_{\text{scat}}, z_{\text{scat}})$ and the closest distance between the two proton track were applied to emphasize the pp scattering. The scattering vertex was required to be $x_{\text{scat}}^2 + y_{\text{scat}}^2 < 25^2, |z_{\text{scat}}| < 170$ in mm unit. The closest distance of the two proton track was required to be less than 10 mm. By projecting Δp spectrum by the momentum region of Σ^+ and scattering angle of the Σ^+ in assuming Σ^+p scattering, the projected Δp spectra were used in the fitting for background estimation, as mentioned in Subsection 4.2.3 (see also Fig. C4 in Appendix C).

As mentioned in Subsection 4.3.2, the angular distribution of the protons from this reaction was compared between the real data and efficiency-corrected simulation to estimate the effect of the uncertainty of the efficiency at the acceptance edge for analysis of two-proton events. Because the angular distribution of the differential cross section of the pp scattering is almost flat, the angular dependence should be the same if the efficiency correction was fine. From Fig. A3, the angular distribution in data was sandwiched with the two efficiency-corrected simulations using the possible lowest and highest CFT tracking efficiencies.

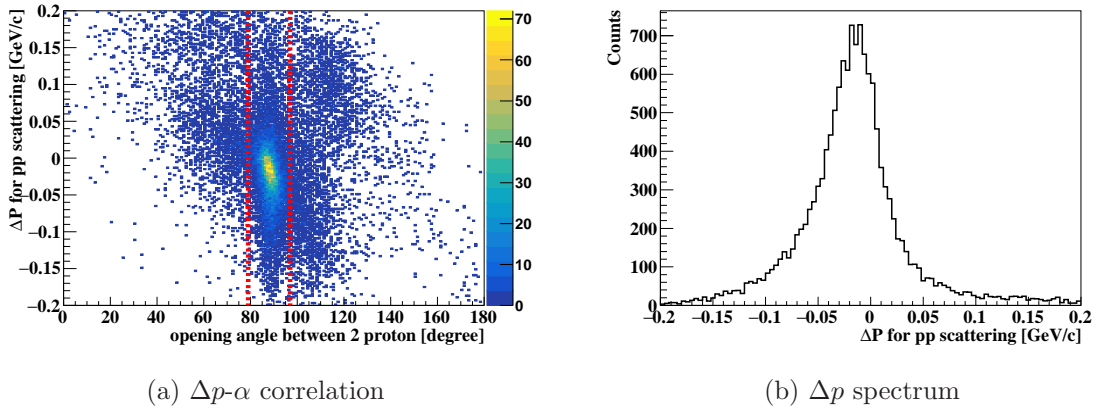


Fig. A2: (a) Correlation of the Δp and the opening angle between two detected proton α (b) Δp spectrum for the two-proton events with cuts to select the pp scattering following $\Sigma^+ \rightarrow p\pi^0$ decay.

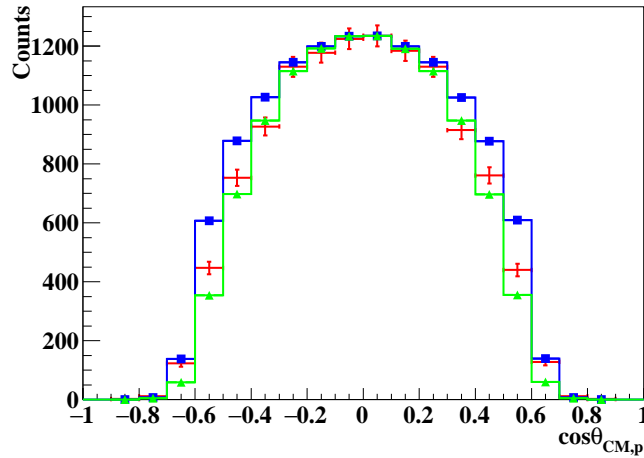


Fig. A3: Angular distribution of the protons from the pp scattering following the $\Sigma^+ \rightarrow p\pi^0$ decay events, where the momentum of the decay proton behaving the beam for the pp scattering was selected as $0.5 < p_{meas}[\text{GeV}/c] < 0.6$. The red points represent the data. The green and blue points show the simulation with the efficiency correction using the possible lowest and highest CFT tracking efficiencies, respectively. The simulations are normalized by the counts of $0 < \cos\theta_{CM,p} < 0.1$ bin.

B Appendix B: Concrete expressions of differential cross section as a function of phase shifts

As the NN scattering case [44], the wave function for the Σ^+p scattering can asymptotically be written as

$$\psi_{m'}^{S'}(\mathbf{r}) \sim e^{ikz} \xi_{m'}^{S'} + \frac{e^{ikr}}{r} \sum_{S,m} \xi_m^S M_{m,m'}^{S,S'}(\theta, \phi) \quad (\text{B1})$$

where k represents the wavenumber of relative motion in the CM system defined as $k = \frac{p_{\text{CM}}}{\hbar}$, ξ_m^S denotes the spin state with spin quantum number m , and $M_{m,m'}^{S,S'}$ are the matrix elements of the spin- $\frac{1}{2}$ spin- $\frac{1}{2}$ scattering amplitude with polar angle θ and azimuthal angle ϕ . By the partial-wave decomposition, the matrix element becomes

$$\begin{aligned} M_{m,m'}^{S,S'}(\theta, \phi) = & \sum_L \sum_{J=|L-S|}^{L+S} \sum_{L'=|J-S'|}^{J+S'} \sqrt{4\pi(2L'+1)} Y_L^{m'-m}(\theta, \phi) \\ & \times C_{L \times S}(J, m', m' - m, m) C_{L' \times S'}(J, m', 0, m') i^{L'-L} \frac{\langle L, S | S^{\text{mat}} - 1 | L', S' \rangle}{2ik} \end{aligned} \quad (\text{B2})$$

where the $C_{L \times S}$ are Clebsch-Gordan coefficients defined as $C_{L \times S}(J, m_J, m_L, m_S) = \langle L m_L S m_S | L S J m_J \rangle$ and Y_L^m is a spherical harmonic. The differential cross section for scattering of an unpolarized beam on an unpolarized target I_0 is expressed by matrix elements as

$$I_0 = \frac{1}{4} |M_{0,0}^{0,0}|^2 + \frac{1}{2} |M_{1,1}^{1,1}|^2 + \frac{1}{4} |M_{0,0}^{1,1}|^2 + \frac{1}{2} |M_{0,1}^{1,1}|^2 + \frac{1}{2} |M_{1,0}^{1,1}|^2 + \frac{1}{2} |M_{1,-1}^{1,1}|^2 \quad (\text{B3})$$

The explicit formulae of matrix elements as a function of the partial wave amplitudes h for general angular momentum L can be found in [45]. The concrete expressions by D-wave

($L \leq 2$) are described as

$$M_{0,0}^{0,0} = h_{1S_0} + 3h_{1P_1} \cos \theta + 5h_{1D_2} \times \left(\frac{3 \cos^2 \theta - 1}{2} \right), \quad (\text{B4})$$

$$M_{1,1}^{1,1} = \left(h_{3S_1} - \frac{\sqrt{2}}{2} h^3 S_1^{-3D_1} \right) + \left(\frac{3}{2} h_{3P_2} + \frac{3}{2} h_{3P_1} \right) \cos \theta \\ + \left(2h_{3D_3} + \frac{5}{2} h_{3D_2} + \frac{1}{2} h_{3D_1} - \frac{\sqrt{2}}{2} h^3 S_1^{-3D_1} \right) \times \frac{3 \cos^2 \theta - 1}{2}, \quad (\text{B5})$$

$$M_{0,0}^{1,1} = (h_{3S_1} + \sqrt{2} h^3 S_1^{-3D_1}) + (2h_{3P_2} + h_{3P_0}) \cos \theta \\ + (3h_{3D_3} + 2h_{3D_1} + \sqrt{2} h^3 S_1^{-3D_1}) \times \frac{3 \cos^2 \theta - 1}{2}, \quad (\text{B6})$$

$$M_{0,1}^{1,1} = \left(-\frac{3}{2\sqrt{2}} h_{3P_2} + \frac{3}{2\sqrt{2}} h_{3P_1} \right) \times (-\sin \theta) \\ + \left(-\frac{4}{3\sqrt{2}} h_{3D_3} + \frac{5}{6\sqrt{2}} h_{3D_2} + \frac{1}{2\sqrt{2}} h_{3D_1} - \frac{1}{\sqrt{2}} h^3 S_1^{-3D_1} \right) \times (-3 \cos \theta \sin \theta), \quad (\text{B7})$$

$$M_{1,0}^{1,1} = \left(\frac{1}{\sqrt{2}} h_{3P_2} - \frac{1}{\sqrt{2}} h_{3P_0} \right) \times (-\sin \theta) \\ + \left(\frac{1}{\sqrt{2}} h_{3D_3} - \frac{1}{\sqrt{2}} h_{3D_1} - \frac{1}{\sqrt{2}} h^3 S_1^{-3D_1} \right) \times (-3 \cos \theta \sin \theta), \quad (\text{B8})$$

$$M_{1,-1}^{1,1} = \left(\frac{1}{6} h_{3D_3} - \frac{5}{12} h_{3D_2} + \frac{1}{4} h_{3D_1} - \frac{1}{2\sqrt{2}} h^3 S_1^{-3D_1} \right) \times (3 \sin^2 \theta), \quad (\text{B9})$$

where partial wave amplitude h were defined as

$$h_{2S+1L_J} = \begin{cases} \frac{1}{2ik} (\cos(2\bar{\epsilon}_1) \exp(2i\bar{\delta}_{2S+1L_J}) - 1) & ({}^3S_1 \text{ and } {}^3D_1 \text{ case}) \\ \frac{1}{2ik} (\exp(2i\bar{\delta}_{2S+1L_J}) - 1) & (\text{otherwise}) \end{cases} \quad (\text{B10})$$

$$h^3 S_1^{-3D_1} = \frac{1}{2k} \sin(2\bar{\epsilon}_1) \exp(i\bar{\delta}_3 S_1 + i\bar{\delta}_3 D_1). \quad (\text{B11})$$

$\bar{\delta}_{2S+1L_J}$ and $\bar{\epsilon}_1$ are the bar-phase shifts, which are strictly different from the commonly used nuclear bar-phase shifts separated from Coulomb effects. Because the energies of the Σ^+p scattering are sufficiently high and the data for very-forward angle is absent, the Coulomb effects might be negligible. Therefore, the bar-phase shifts were equated with the nuclear bar-phase shifts and called merely ‘‘phase shifts δ ’’ in text.

C Appendix C: Angular dependence of the $\Delta E(\Sigma^+p)$ distribution

The fitting results of the ΔE spectra for each scattering angle and momentum region of Σ^+ are shown in Fig. C1, C2, and C3. These fittings were performed under the condition in which cut conditions for Δp spectra were almost the same cut conditions as the ΔE

spectra, except for the kinamatical cuts for pp scattering, that is the Δp and α cuts described in Appendix A. The $\Delta E(\Sigma^+p)$ spectrum can be reproduced by the sum of the simulated spectra. The fitting results of the Δp spectra for low momentum region are also shown in Fig. C4.

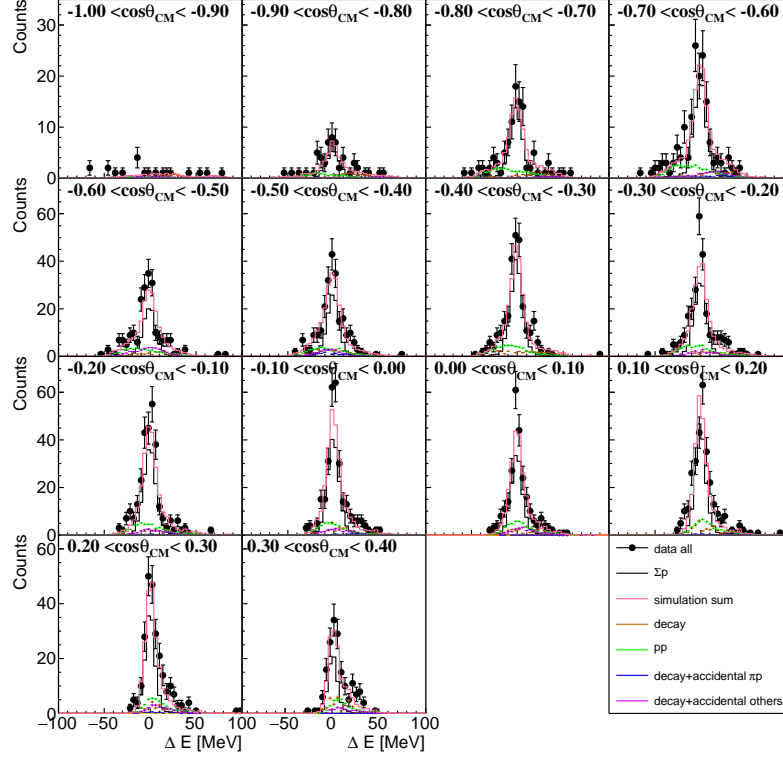


Fig. C1: Fitting results of the ΔE spectra for each scattering angle of Σ^+ in the low momentum region ($p_\Sigma[\text{GeV}/c] < 0.55$). Data points with error bars show the experimental data. Simulated spectra for the assumed reactions are also shown and the histogram with a red line showing the sum of these spectra.

D Appendix D: Table of the differential cross sections

The values of the differential cross sections and their uncertainty are summarized in Tables D1, D2, and D3.

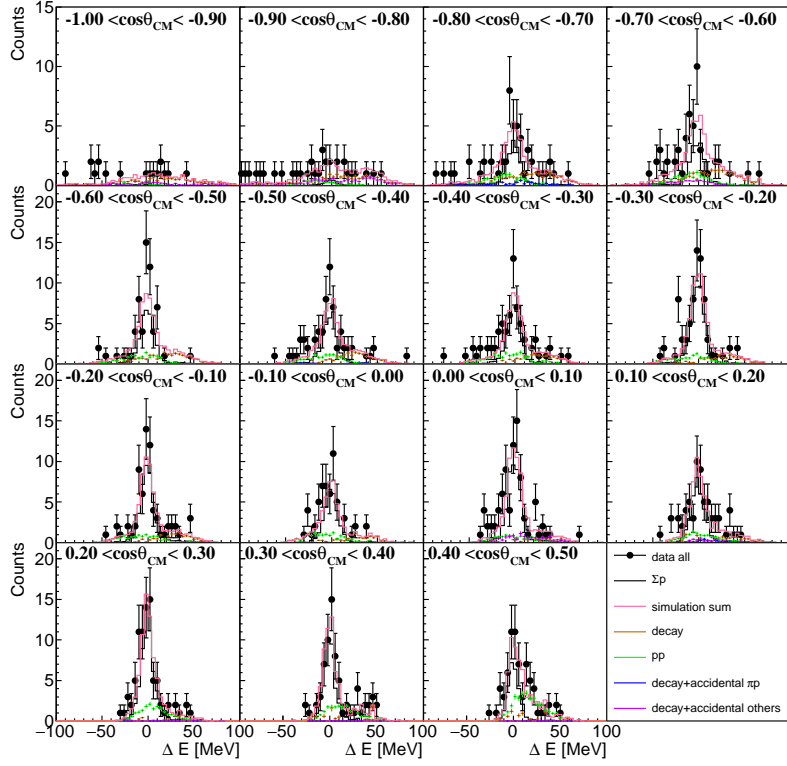


Fig. C2: Fitting results of the ΔE spectra for each scattering angle of Σ^+ in the middle momentum region ($0.55 < p_\Sigma [\text{GeV}/c] < 0.65$). The data points and histograms are the same as those in Fig. C1.

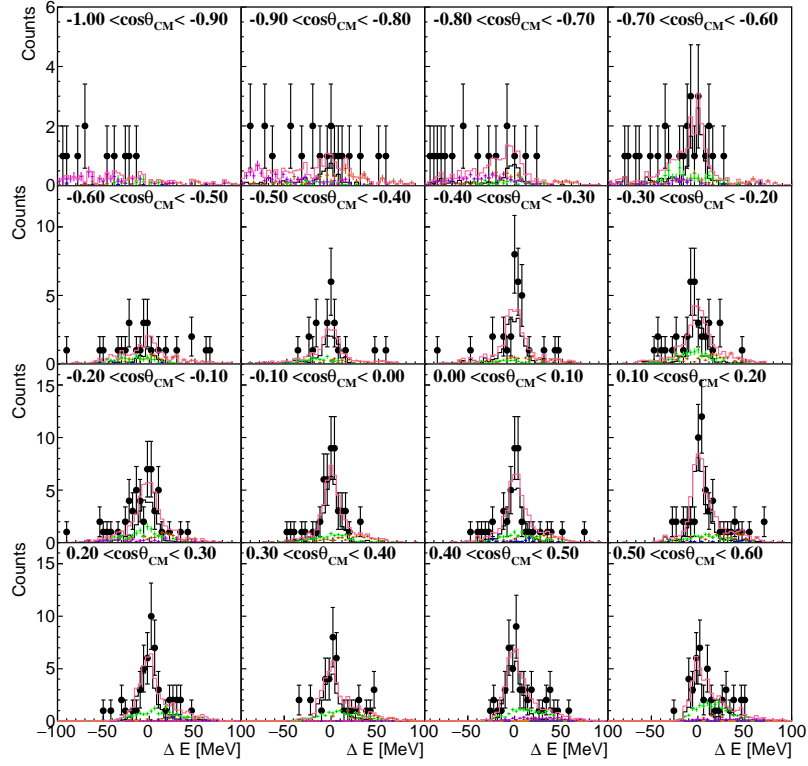


Fig. C3: Fitting results of the ΔE spectra for each scattering angle of Σ^+ in the high momentum region ($0.65 < p_{\Sigma}[\text{GeV}/c] < 0.80$). The data points and histograms are the same as those in Fig. C1.

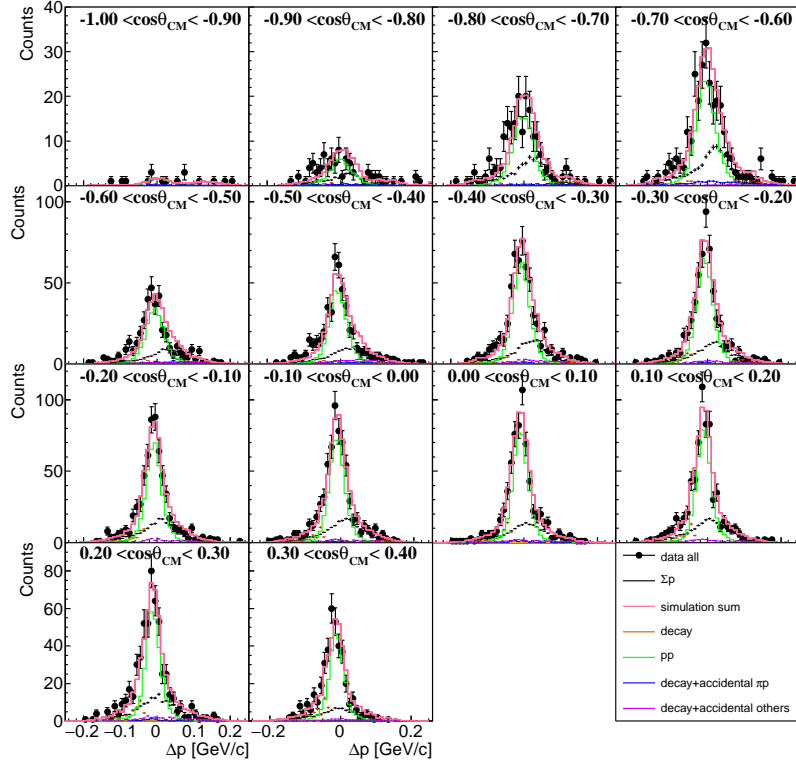


Fig. C4: Fitting results of the Δp spectra for each scattering angle in the low momentum region ($p_{\Sigma}[\text{GeV}/c] < 0.55$). The data points and histograms are the same as those in Fig. C1.

Table D1: Values and errors of the differential cross section of the Σ^+p elastic scattering for the low momentum region ($0.44 < p_\Sigma[\text{GeV}/c] < 0.55$). The systematic error is estimated as a quadratic sum of the error from the background estimation, averaged efficiency, and Σ^+ total flight length.

$\cos \theta_{\text{CM}}$	$\frac{d\sigma}{d\Omega}$ [mb/sr]	stat. [mb/sr]	syst. (Total) [mb/sr]	syst. (BG) [mb/sr]	syst. (eff) [mb/sr]	syst. (L) [mb/sr]
-0.85 ± 0.05	2.22	± 0.46	± 0.38	± 0.20	± 0.32	± 0.04
-0.75 ± 0.05	2.31	± 0.32	± 0.32	± 0.14	± 0.28	± 0.05
-0.65 ± 0.05	2.12	± 0.26	± 0.28	± 0.17	± 0.22	± 0.04
-0.55 ± 0.05	2.00	± 0.29	± 0.37	± 0.33	± 0.17	± 0.04
-0.45 ± 0.05	1.93	± 0.27	± 0.40	± 0.38	± 0.13	± 0.04
-0.35 ± 0.05	2.40	± 0.22	± 0.20	± 0.12	± 0.15	± 0.05
-0.25 ± 0.05	1.92	± 0.19	± 0.23	± 0.17	± 0.15	± 0.04
-0.15 ± 0.05	2.22	± 0.19	± 0.29	± 0.23	± 0.17	± 0.04
-0.05 ± 0.05	2.22	± 0.19	± 0.26	± 0.15	± 0.21	± 0.04
0.05 ± 0.05	1.86	± 0.21	± 0.22	± 0.09	± 0.20	± 0.04
0.15 ± 0.05	2.54	± 0.23	± 0.37	± 0.10	± 0.35	± 0.05
0.25 ± 0.05	2.84	± 0.29	± 0.57	± 0.14	± 0.55	± 0.06
0.35 ± 0.05	3.02	± 0.51	± 0.89	± 0.19	± 0.86	± 0.06

Table D2: Values and errors of the differential cross section of the Σ^+p elastic scattering for the middle momentum region ($0.55 < p_\Sigma[\text{GeV}/c] < 0.65$).

$\cos \theta_{\text{CM}}$	$\frac{d\sigma}{d\Omega}$	stat.	syst. (Total)	syst. (BG)	syst. (eff)	syst. (L)
	[mb/sr]	[mb/sr]	[mb/sr]	[mb/sr]	[mb/sr]	[mb/sr]
-0.75 ± 0.05	1.24	± 0.38	± 0.20	± 0.15	± 0.13	± 0.02
-0.65 ± 0.05	0.90	± 0.38	± 0.14	± 0.12	± 0.07	± 0.02
-0.55 ± 0.05	1.73	± 0.32	± 0.19	± 0.17	± 0.08	± 0.03
-0.45 ± 0.05	1.24	± 0.28	± 0.06	± 0.03	± 0.04	± 0.02
-0.35 ± 0.05	1.35	± 0.27	± 0.10	± 0.08	± 0.05	± 0.03
-0.25 ± 0.05	1.79	± 0.28	± 0.08	± 0.05	± 0.05	± 0.04
-0.15 ± 0.05	1.42	± 0.23	± 0.06	± 0.04	± 0.02	± 0.03
-0.05 ± 0.05	1.07	± 0.21	± 0.09	± 0.08	± 0.02	± 0.02
0.05 ± 0.05	1.70	± 0.29	± 0.08	± 0.05	± 0.05	± 0.03
0.15 ± 0.05	1.11	± 0.29	± 0.11	± 0.09	± 0.05	± 0.02
0.25 ± 0.05	2.34	± 0.37	± 0.16	± 0.04	± 0.15	± 0.05
0.35 ± 0.05	2.00	± 0.39	± 0.20	± 0.06	± 0.19	± 0.04
0.45 ± 0.05	2.25	± 0.53	± 0.43	± 0.15	± 0.40	± 0.05

Table D3: Values and errors of the differential cross section of the Σ^+p elastic scattering for the high momentum region ($0.65 < p_\Sigma[\text{GeV}/c] < 0.80$).

$\cos \theta_{\text{CM}}$	$\frac{d\sigma}{d\Omega}$	stat.	syst. (Total)	syst. (BG)	syst. (eff)	syst. (L)
	[mb/sr]	[mb/sr]	[mb/sr]	[mb/sr]	[mb/sr]	[mb/sr]
-0.85 ± 0.05	0.81	± 0.52	± 0.10	± 0.04	± 0.09	± 0.01
-0.75 ± 0.05	0.58	± 0.39	± 0.05	± 0.02	± 0.04	± 0.01
-0.65 ± 0.05	1.26	± 0.42	± 0.10	± 0.08	± 0.06	± 0.02
-0.55 ± 0.05	0.68	± 0.34	± 0.12	± 0.11	± 0.02	± 0.01
-0.45 ± 0.05	1.08	± 0.33	± 0.07	± 0.07	± 0.02	± 0.02
-0.35 ± 0.05	1.35	± 0.31	± 0.04	± 0.03	± 0.02	± 0.02
-0.25 ± 0.05	1.29	± 0.35	± 0.10	± 0.10	± 0.02	± 0.02
-0.15 ± 0.05	1.58	± 0.44	± 0.06	± 0.06	± 0.01	± 0.02
-0.05 ± 0.05	2.08	± 0.40	± 0.18	± 0.17	± 0.06	± 0.03
0.05 ± 0.05	1.50	± 0.37	± 0.21	± 0.20	± 0.06	± 0.02
0.15 ± 0.05	2.40	± 0.47	± 0.22	± 0.19	± 0.10	± 0.04
0.25 ± 0.05	2.02	± 0.45	± 0.10	± 0.07	± 0.06	± 0.03
0.35 ± 0.05	1.47	± 0.43	± 0.24	± 0.23	± 0.06	± 0.02
0.45 ± 0.05	1.90	± 0.44	± 0.28	± 0.26	± 0.11	± 0.03
0.55 ± 0.05	1.70	± 0.52	± 0.19	± 0.04	± 0.18	± 0.03